*J. Fluid Mech.* (2002), *vol.* 454, *pp.* 113–144. © 2002 Cambridge University Press 
DOI: 10.1017/S0022112001007005 Printed in the United Kingdom

# Experimental study of a jet in a crossflow at very low Reynolds number

By R. CAMUSSI, G. GUJ AND A. STELLA

Dipartimento Ingegneria Meccanica e Industriale,
Universitá 'Roma Tre', Via della Vasca Navale 79, 00146 Rome, Italy

(Received 20 October 2000 and in revised form 12 September 2001)

Flow visualizations and phase-averaged particle image velocimetry (PIV) measurements of a jet in crossflow configuration at very low Reynolds numbers ($Re_j \simeq 100$) are performed in a water tunnel for jet-to-cross-stream velocity ratios $R$ ranging from 1.5 to 4.5. The PIV vector fields and flow visualizations, carried out by injecting methylene blue dye and by the laser induced fluorescence (LIF) technique, are analysed to characterize the effect of $R$ on the formation and evolution of large-scale vortices. It is shown that two distinct flow regimes are established depending on $R$, with $R \simeq 3$ being a transitional value. At low $R$, the longitudinal vorticity dynamics is dominated by the so-called wake-like structures which are shown to be strictly connected to the streamwise counter-rotating vortices (CRVP) which drive the destabilization of the jet flow. On the other hand, at large $R$, vortices with positive and negative vorticity are coupled together. The establishment of these different behaviours is interpreted physically as an effect of the jet Reynolds number which plays an essential role on the destabilization mechanisms which lead to the formation of the jet shear-layer structures. In any case, the onset of instability is driven by mechanisms which are different from those characteristic of free jets.

## 1. Introduction

The case of jets exhausting in crossflows is important either from the engineering viewpoint, being very frequent in practical applications (e.g. injectors for cooling systems, jets for V-STOL aircraft, smoke exhaust from refineries, exhaust of vehicles) or for basic research, because of the variety of fluid dynamic phenomena involved. The analysis of the flow structures characterizing crossflows is therefore important and, although several works have been recently devoted to this subject (see e.g. Kelso, Lim & Perry 1996 and references therein) further studies are needed because of the complexity of the phenomenon, which is not yet completely understood.

Beyond the complex dynamics, difficulties in studying this subject are also related to the combined effects of two main independent non-dimensional parameters which influence the physical behaviour. The first one is a typical Reynolds number which is usually assumed to characterize crossflows. It is denoted as $Re_j = U_\infty D_j/\nu$, therefore defined on the basis of the jet diameter $D_j$ and the cross-stream velocity $U_\infty$, assuming that the two fluids have the same kinematic viscosity $\nu$. The information concerning the jet velocity is achieved by the so-called effective velocity ratio $R$ defined as the ratio between the jet and the cross-stream momenta. If the working fluids of the two streams are the same and isothermal, as in the present case, this parameter reduces to $R = U_j/U_\infty$.

https://doi.org/10.1017/S0022112001007005 Published online by Cambridge University Press

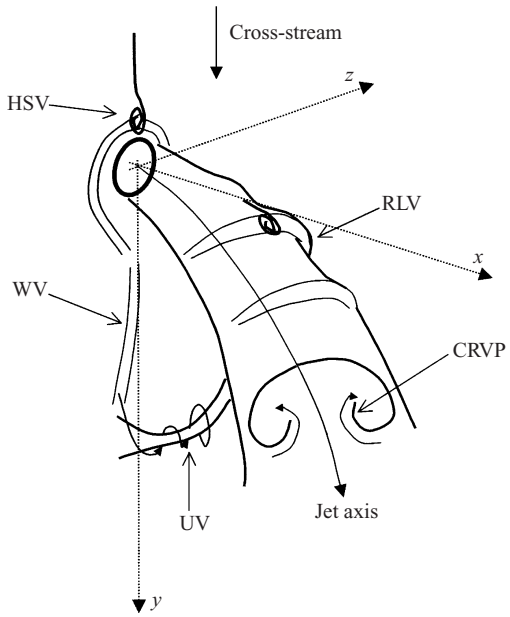



FIGURE 1. A schematic diagram of the main vortical structures formed in a jet issuing in a crossflow.

As indicated, for example, by Fric & Roshko (1994), a simplified view of the physical phenomenon may give an indication of the basic coherent structures or vortex systems which are formed from the interaction of the jet flow with the cross-stream. A sketch of the phenomenology is given in figure 1 (see also figure 1 of Kelso *et al.* 1996). With reference to this scheme, we may attempt to classify the main structures as follows:

Class 1. Structures which are originated by the interaction of the jet with the crossflow and the wall, and which cannot be recognized in free jets. Among structures of this kind we may include the following vortex systems (Andreopulos & Rodi 1984):
CRVP: the counter-rotating vortex pair, which is originated as an effect of the bending of the jet itself (see also Broadwell & Breidenthal 1984).
HSV: the horseshoe vortices, formed upstream of the jet and close to the wall (see also Krothapalli, Lourenco & Buchlin 1990).
WV: the wall vortices, which develop downstream of the jet orifice and close to the wall (see e.g. the early work by McMahon, Hester & Palfery 1971).
UV: the upright vortices, which are generated by the interaction of the wall boundary layer with the jet flow and which, for low $Re_j$, are the only unsteady structures (see e.g. Fric & Roshko 1994; Kelso *et al.* 1996).

Class 2. Structures which are proper for free jets, but whose vorticity content, evolution and destabilization are in some way influenced by the presence of the crossflow. Structures of this kind are:
RLV: the ring-like vortices, which are formed from the shear layer of the jet flow and whose shape and spatial evolution is distorted by the presence of the cross-stream.

The CRVP of class 1 and the RLV of class 2 determine the dominant features of the velocity and vorticity fields and their dynamics is of great interest from the practical viewpoint since they are mainly responsible for mixing, and for mass, momentum and heat transfer (see Kamotani & Greber 1972; Fornalik *et al.* 1999). In the present work,

https://doi.org/10.1017/S0022112001007005 Published online by Cambridge University Press

we focus attention on such vortex systems and on their reciprocal influence. Indeed, their interactions give rise to complicated behaviours which are not yet completely understood mainly for what concerns the instability mechanisms and the transition to a turbulent state.

Many experimental studies have been carried out by means of flow visualizations (see e.g. Kelso *et al.* 1996) which are of fundamental importance for preliminary understanding of the main physical behaviour even if they lead only to qualitative results and sometimes offer multiple interpretations. On the other hand, image-processing techniques can deliver quantitative information about the flow. The particle image velocimetry (PIV) technique offers such a possibility not only yielding planar velocity fields but, as pointed out by Adrian (1991), also providing a good connection between the clear features observed by visualizations, and the need for a quantification of the velocity or vorticity magnitudes. As far as we know, previous studies of jets in crossflow configuration have been conducted using the PIV technique only for studying global features (e.g. Cenedese & De Angelis 1998) whereas no quantitative studies concerning coherent structure properties have been conducted so far using the PIV methodology. Most of the previous experimental quantitative analyses were, in fact, based on pointwise hot-wire anemometry measurements (using a probe with a single wire, e.g. by Moussa, Trischka & Eskinazi 1977, or X wire, e.g. by Andreopulos 1985; or triple wires, e.g. by Andreopulos & Rodi 1984), by using rakes of probes (e.g. Fearn & Weston 1974), or on concentration measurements (Smith & Mungal 1998; Blanchard, Brunet & Merlen 1999). Of relevance for present purposes is the work by Kelso *et al.* (1996), which, adopting hot wires on moving devices, offers phase-averaged data which show features similar to those obtained in the present study, but at larger Reynolds number.

The main purpose of the present work is to extend to very low $Re_j$ ($Re_j \simeq 100$) previous experimental analyses on structures of both classes 1 and 2, and, in particular, to characterize in a quantitative manner both the RLV and the CRVP physical properties and their mutual interactions. These tasks are here pursued by an experimental analysis which is based both on flow visualizations and on PIV measurements. The results achieved are compared with previous studies at higher $Re_j$ and with the mechanisms usually observed in free jets. The present analysis, and specifically the choice of very low $Re$, is motivated by the lack of results in such flow conditions. The results may be of interest for comparison with numerical simulations still not affordable at high $Re$. Furthermore, the low velocities (and larger typical time scales) of the present experiment permit the clear observation of vorticity dynamics which are difficult to study at larger velocity conditions.

In the present work, a technique for phase averaging and conditional PIV image acquisitions based on mechanical forcing of the issuing jet has been developed also. As will be described later in detail, the forcing is synchronized with PIV image acquisition, permitting the analysis of the mean velocity and vorticity fields by ensemble averages. The conditional acquisitions are conducted for different $R$ and adopting two different orientations of the measurement section: a plane perpendicular to the wall of the principal duct and containing the jet axis, hereinafter denoted as the longitudinal section; and a plane parallel to the wall and at different distances from it, denoted as the transverse section. The analysis of the velocity and vorticity fields on two orthogonal planes, but acquired at the same phase, allows for structures of different kinds to be related to each other. In particular, the adopted conditioning procedure permits us to shed some light on the connection between the CRVP and the RLV, an aspect which, owing to the distribution of vorticity on different planes, is very difficult

https://doi.org/10.1017/S0022112001007005 Published online by Cambridge University Press

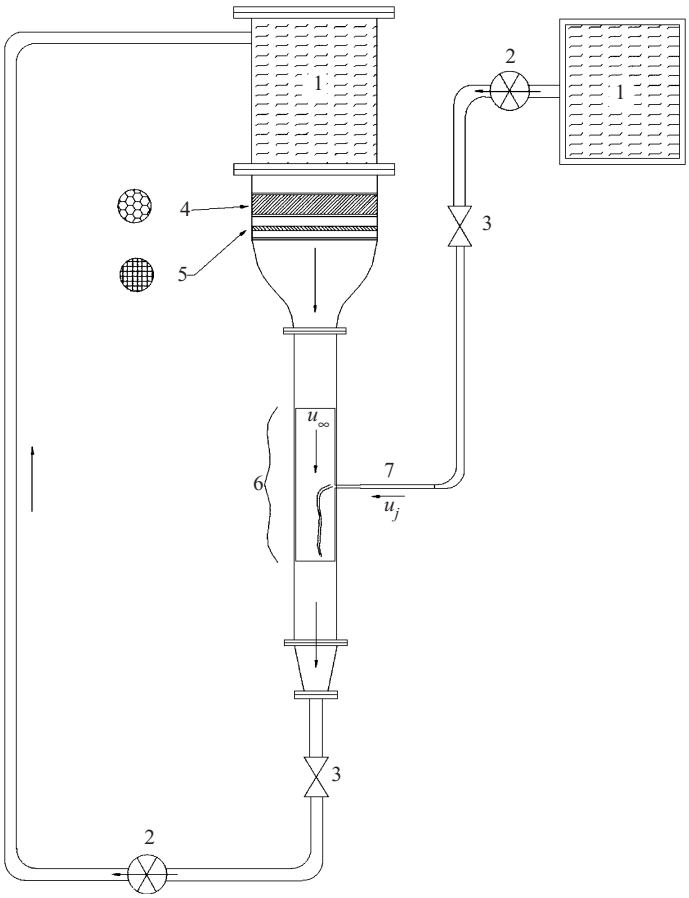



FIGURE 2. A scheme of the experimental appratus and the main components. 1, water reservoir; 2, water pump; 3, flow meter and flowrate regulator; 4, honeycomb; 5, screen series; 6, test section (Plexiglas window); 7, small pipe (perpendicular to 6).

to study with no phase conditioning. In light of such information, and accounting also for the flow visualization results, the overall three-dimensional physical features are inferred and analysed in detail.

The paper is organized as follows. In § 2, the experimental facility is described, as well as the procedures adopted for flow visualizations and the PIV acquisitions without forcing. The conditional averaging technique applied when the forcing was active, is described in § 3. Results are presented in § 4, and the effect of $R$ on the onset on instability is described in § 5. Final remarks and conclusions are summarized in § 6.

## 2. Experimental set-up and techniques

### 2.1. *Experimental facility*

The experimental analysis is performed in a gravity-driven water tunnel (figure 2) available at the aerodynamics laboratory of the Department of Mechanics and Aeronautics, of the University of Rome 'La Sapienza'. The still chamber, equipped with honeycomb and screens, is followed by a contraction, with a ratio of 10, which acceler-

https://doi.org/10.1017/S0022112001007005 Published online by Cambridge University Press

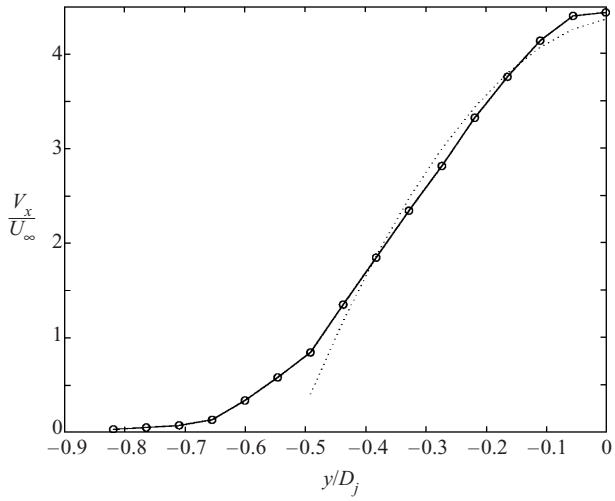



FIGURE 3. Half velocity profile close to the jet exit computed from averaging 10 PIV results at $R \simeq 3$ and $x/D_j = 1$. $V_x$ is the velocity component along the $x$-axis. Dotted line is a parabolic fit computed in the range $-0.5 \leqslant y/D_j \leqslant 0$.

ates the water flow into the square test section ($0.1\,\mathrm{m} \times 0.1\,\mathrm{m} \times 1.0\,\mathrm{m}$). The cross-water jet with circular section of 5 mm diameter is flush mounted in the middle of the test section, perpendicular to the wall and is gravity driven by an independent reservoir. The mean velocities of the free stream and of the jet flow are exactly metered by means of proper flow meters. The free-stream velocity ($U_\infty$) is fixed to $0.02\,\mathrm{m\,s^{-1}}$ and the corresponding $Re_j$ is 100. The velocity ratio $R$ is varied in the range 1.5–4.5, only by changing the jet velocity.

### 2.2. *Flow qualification*

Preliminary PIV measurements have been conducted for the validation of the quality characteristics of the two flows: the main free stream and the jet. Also, analyses have been performed to substantiate the experimental findings for the inflow boundary conditions.

The quality of the main stream has been quantified in terms of flow uniformity, turbulence levels and boundary-layer thickness and conditions. The flow uniformity and turbulence levels have been evaluated, as performed in large wind or water tunnel test sections, by the spatial $\sigma_s$ and temporal $\sigma_t$ standard deviations using a number of samples of the order of 5000. These values are $\sigma_s = 0.3\,\mathrm{mm\,s^{-1}}$ and $\sigma_t = 0.8\,\mathrm{mm\,s^{-1}}$ which correspond to turbulence levels $\sigma_s/U_\infty = 0.015$ and $\sigma_t/U_\infty = 0.04$, respectively. We have to observe that $\sigma_t$ is of the order of the resolution of the adopted PIV configuration, and so we can guess that the actual values should be even smaller.

The boundary layer on the wall of the test section is laminar and stationary according to $Re_x \simeq 10^4$, which is more than one order of magnitude less than the critical value. The displacement thickness ($\delta^*$), computed by integrating the von Kármán–Polausen equation from the anti-turbulence screen in the still chamber to the measurement section, is equal to 7.2 mm. The spatial and dynamical resolution of the PIV velocity fields and the presence of the optical noise due to wall light refraction do not allow the actual boundary-layer velocity profile to be accurately measured, even if it seems smaller than the theoretical one.

The velocity profile of the jet, obtained by averaging a number of 10 PIV results

https://doi.org/10.1017/S0022112001007005 Published online by Cambridge University Press

5 mm from the wall, is parabolic (figure 3), confirming the fully developed laminar conditions. This result is in agreement with the theoretical findings, since the parameter $Re_{jet} = R \times Re_j$, is in the range 150–450, that is about five times smaller than the critical value for pipes of circular section.

During both the visualizations and the PIV measurements, the jet and the free-stream fluid temperatures are monitored in order to stop the experiment as soon as buoyancy effects tend to affect the behaviour of the flow. The temperature of the flows is maintained at $24 \pm 1\,^{\circ}\mathrm{C}$. Also, the buoyancy effect related to the dyes used for the flow visualizations and the seeding for the PIV measurements are checked to be negligible and the Schmidt number $Sc$ of the adopted tracers to be large enough ($Sc = \nu/k_c \simeq 1000$ where $k_c$ is the diffusion coefficient).

### 2.3. *Flow-visualization techniques*

Two types of flow visualization were carried out. In the first case, visualizations were performed by mixing fluorescein with the water within the reservoir which drives the jet. In this way, only the jet flow was visualized in two-dimensional planes. Planar sections were illuminated via a laser light sheet produced by a continuous 2 W laser source *Innova 70* (wavelength $\lambda = 513\,\mu\mathrm{m}$) passing through a cylindrical lens so that the thickness of the achieved light sheet ($d$) was of about 2 mm. A fibre optic of suitable length, mounted on a system with micrometric regulators, allowed the laser sheet to be oriented in several positions. A schematic representation of the illuminating set-up is shown in figure 4. The laser sheet has been positioned in the $O$-$x, y$ plane, containing the jet axis, to analyse the longitudinal fields associated to the RLV, and on planes parallel to the $O$-$y, z$ plane, referred to as transverse pictures, for the analysis of the CRVP.

The second campaign of flow visualizations was performed using methylene blue dye in order for three-dimensional structures to be qualitatively identified. In this case, a white light source was used and, as for the LIF method, dye was injected directly inside the jet. In order for wall structures to be analysed, 4 holes of 0.5 mm diameter were made around the jet orifice. Methylene blue dye was injected through small needles inserted through these holes. The ducts feeding each needle could be opened or closed independently of the others. The presence of the small holes did not affect the free-stream conditions or the boundary-layer thickness.

Video tape recordings, by means of a CCD monochrome video camera SONY XC-77RR-CE, and photo pictures, by means a programmable camera CANON T90, were performed both when dye and fluorescein were used.

### 2.4. *PIV technique*

#### 2.4.1. *Imaging configuration and hardware*

The configuration adopted for the illumination of the measurement plane is the same as that used for LIF analysis presented in figure 4. Flow seeding was achieved by tracer particles of lycopodium with a mean diameter $D = 30\,\mu\mathrm{m}$ and a particle to fluid density ratio $\rho_p/\rho_f$ equal to 0.31. The particles were added both to the jet and the cross-stream.

The CCD video camera (already mentioned in § 2.3) and a frame grabber board connected to a standard PC are used to capture and acquire images of the illuminated particles in the observation area. The camera presents a resolution of $756 \times 512$ pixels, with a size of $11 \times 11\,\mu\mathrm{m}$. It operates in the interlaced frame integration mode, in

https://doi.org/10.1017/S0022112001007005 Published online by Cambridge University Press

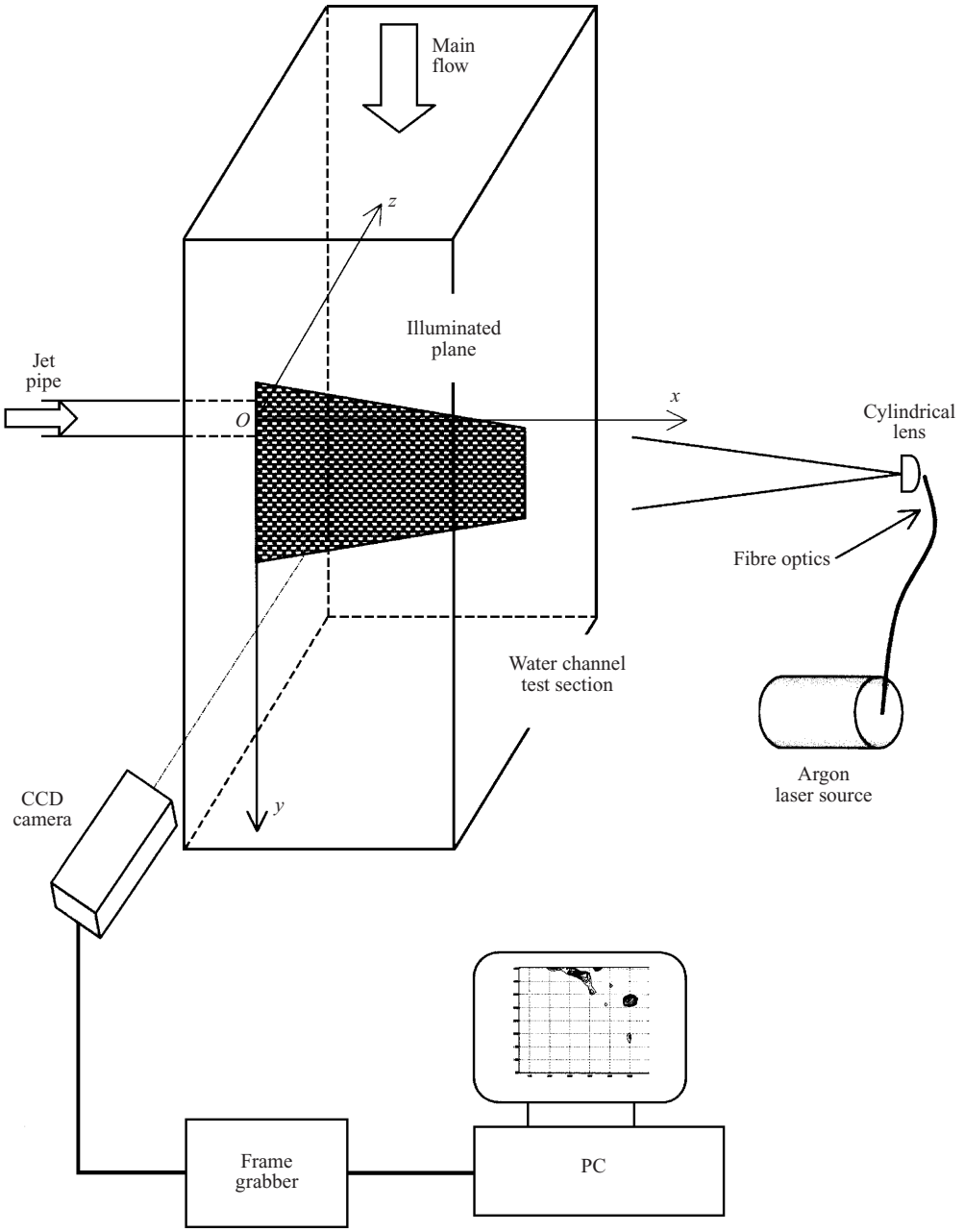



FIGURE 4. The set-up for the LIF visualizations and PIV measurements.

which the odd and even lines of one frame are separated into two images. Although this mode reduces the spatial resolution, owing to the interpolation used to replace the missing lines, it allows the velocity sign to be retrieved by adopting a cross-correlation post-processing procedure. The shutter time $\Delta t$ between odd and even lines has been varied depending on $R$ within the range 9–15 ms. The images captured by the camera are acquired on-line by the 8-bit A/D converter of a VFG-100 image-processing board. For the purposes of conditional PIV acquisition, a sequence of 4 images, with

https://doi.org/10.1017/S0022112001007005 Published online by Cambridge University Press

a selectable time interval, is stored in a buffer using an initial resolution of 6 bits, then extended to 8 bits through zero-padding.

2.4.2. *Image evaluation and spatial resolution*

A velocity vector is evaluated in an interrogation window (IW) as the ratio between the averaged displacement of the particles and $\Delta t$. Particle displacement within an IW is evaluated applying a cross-correlation technique (Willert & Gharib 1991; Raffel, Willert & Kompenhans 1998), based on a two-dimensional discrete Fourier transform. In order to improve the signal to noise ratio, images are pre-processed to produce a quasi-binary image by equalizing the variation of the particle intensity (the so-called local image binarization procedure, Hiller *et al.* 1993). IW sizes of $48 \times 32$ pixels and $24 \times 16$ pixels, 75% overlapped, are used for the evaluation of the longitudinal and transversal recordings. Hence, the distance between two adjacent vectors in the physical space is in the range 0.8–1.3 mm.

2.4.3. *Measurement accuracy*

The measurement accuracy is connected mainly to three causes, that is, limited dynamic range, large out-of-plane velocity components and seeding tracking effect.

The velocity dynamic range can be expressed in terms of particle displacements, which are determined with a resolution of $\frac{1}{2}$ pixel through interpolation, and correspond to about 0.05 mm. The minimum velocity $V_{min}$ that the system is able to resolve is given by the ratio between the minimum detectable displacement and $\Delta t$. For the present measurements, we have $V_{min} = 2.5\,\mathrm{mm\,s^{-1}}$. The maximum displacement detectable by FFT-based PIV evaluation is limited by the IW size and should not exceed $\frac{1}{4}$ of the IW (see Keane & Adrian 1992; Raffel *et al.* 1998) in the ideal case. This condition corresponds to a maximum resolvable velocity $V_{max}$ of about $58\,\mathrm{mm\,s^{-1}}$ for the longitudinal measurements and $27\,\mathrm{mm\,s^{-1}}$ for the transversal ones. The most critical conditions for PIV evaluation of the present recordings occur in the longitudinal acquisitions, in correspondence either of the jet core or of the jet shear layer, owing to the large velocity and gradient of velocity present. As a matter of fact, the majority of non-physical vectors (outliers) are noticed in the two aforementioned regions. The outliers are recognized based on the criterion of a threshold dependent on the $R$ magnitude and therefore are replaced by the average of the surrounding vectors. Indicatively, for $R = 4$, the percentage of spurious vectors does not exceed 5%.

The signal-to-noise ratio is also affected by the presence of an out-of-plane velocity component, which conveys particles across the light sheet. This fact introduces optical noise due to particle appearance and disappearance between the first and second image (Raffel *et al.* 1998). In the present measurement campaign, the effect of the out-of-plane velocity component can be relevant when measuring transversal fields, especially in those regions crossed by the jet flow. The associated measurement uncertainty can be assessed on the basis of the fraction of particles appearing and disappearing, denoted by $P$, that is calculated as the ratio between particle displacement in the direction normal to the light sheet and $d$ (the sheet thickness). The maximum local $P$ is in the range 0.37–0.75 for $2 \leqslant R \leqslant 4$ and occurs in the jet core section. This effect has been previously tested (Quenot, Pakleza & Kowalewski 1998) using synthetic images for $P$ up to 0.2. The maximum error has been found to be below 3% for the angle measurement and 2.5% for the absolute displacement measurement. Of course, the uncertainty will be larger in the present conditions, especially as $R$ increases, but it affects substantially only those few IWs covering the jet core section.

https://doi.org/10.1017/S0022112001007005 Published online by Cambridge University Press

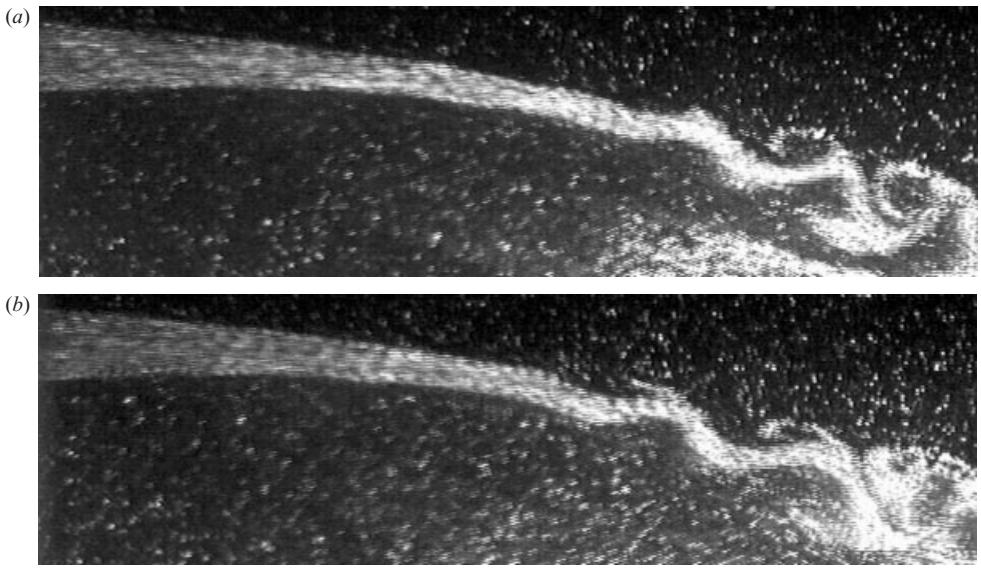



FIGURE 5. Comparison between (*a*) forced and (*b*) unforced visualizations (Mie scattering) obtained at $R \simeq 4$. The forcing does not affect the destabilization position of the jet or the wavelength and amplitude of the oscillations.

The dependency of measurement uncertainty on the seeding tracking performances is less stringent. The terminal velocity is $V_g = 0.34\,\mathrm{mm\,s^{-1}}$ and the relaxation time is $\tau = 1.5 \times 10^{-5}\,\mathrm{s}$. The above values are satisfactory, since $V_g$ is about 1.5% of the mean stream velocity and $\tau$ corresponds to a cut-off frequency of 6.7 kHz, well above the interesting characteristic frequencies.

## 3. Conditional acquisition and post-processing procedures

A conditional acquisition procedure has been implemented in order to capture particle images phase-locked with coherent structure position and generation and to reduce the effects of turbulence and background noise. The averaging procedure leaves the fluid dynamic behaviour of the jet flow unmodified. Therefore, hereinafter, only averaged fields obtained from around 10 PIV results, at the same phase and flow conditions, will be presented. The conditional procedure required a periodic velocity perturbation in the upstream flow of the jet to be applied with a frequency ($f_D$), which is equal to that of the natural preferred mode of destabilization (or its multiple), determined experimentally. In particular, the proper excitation frequencies, for each considered $R$, are selected by tuning the forcing perturbation frequency as far as the topology of the forced flow exactly matches that of the natural case. For example, in figure 5, the forced and unforced Mie scattering visualizations at $R = 4$ are reported. The PIV velocity fields, not presented, allow the velocity components along the streamlines to be evaluated, showing that the wavelengths and amplitudes in the two cases are about the same. In figure 6, a comparison between the forced and the unforced case at $R \simeq 2$ in terms of jet axis curvature (computed from the streamline originated from the jet exit) and velocity component along the $x$-axis is reported, showing good agreement up to a distance from the jet exit of about 7 diameters. The different phase of the unforced case oscillations explains why the conditional

https://doi.org/10.1017/S0022112001007005 Published online by Cambridge University Press

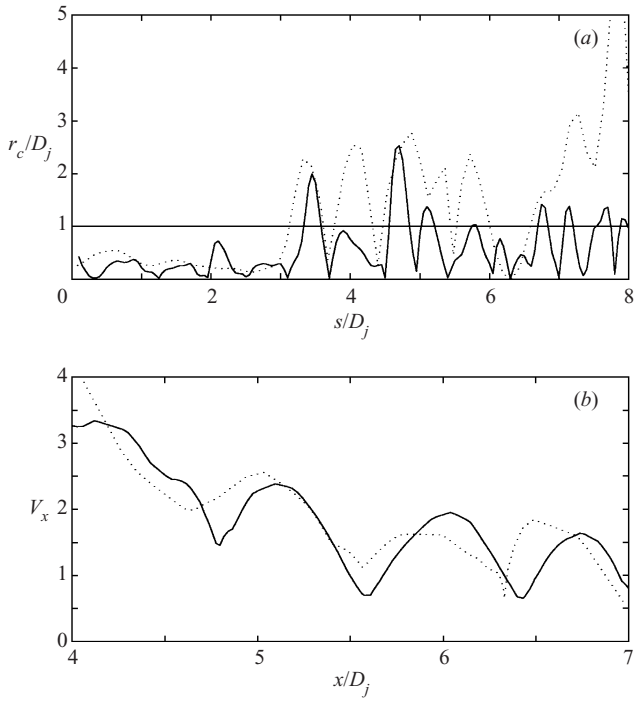



FIGURE 6. Effect of forcing at $R \simeq 2.2$. (*a*) Curvature radius ($r_c$) as a function of the curvilinear abscissa ($s$) of the streamline originating from the jet exit. (*b*) Velocity component along $x$ computed along the same streamline as (*a*). ——, forced case; . . . , unforced.

acquisition has to be implemented. The Strouhal number $St = f_D D/U_J$ of the velocity oscillations can be calculated from figure 6(*b*) by dimensional considerations and results of the order of 0.3, which equals the characteristic value for the destabilization mode of the jet leading to the formation of the RLV. The selected values of $St$, which are more effective in the destabilization of natural modes, are 0.32 and 0.63. To quantify from a statistical point of view the strength of the forcing and its effect on the oscillating flow, the turbulence levels of both forced and unforced conditions are measured. The dimensionless differences are 0.5% and 2.0% taking as reference quantity the mean velocity and the unforced fluctuating velocity, respectively. The relative strength for larger $R$ is smaller, owing to the constant intensity of the mechanical periodical perturbation imposed.

The sketch of the instrumentation set-up for PIV conditional acquisition is shown in figure 7. Synchronization between jet external forcing and image capturing is managed via software. The procedure foresees the acquisition of the external synchronization signal provided by the CCD video camera module. Based on this, a trigger condition is supplied to a signal generator through its external triggering port. The trigger signal starts the generation of a square wavetrain with the appropriate $f_D$. Perturbation of the jet upstream velocity is accomplished by means of a mechanical device, locally squeezing a flexible pipe connected to the jet. The time interval between the beginning of the jet excitation and the first image acquisition is fixed at 10 s for all the test cases. The delay among each of the four images of a sequence, which determines the phase-delay between acquired images and coherent structure positions, is varied in the range 100–300 ms.

https://doi.org/10.1017/S0022112001007005 Published online by Cambridge University Press

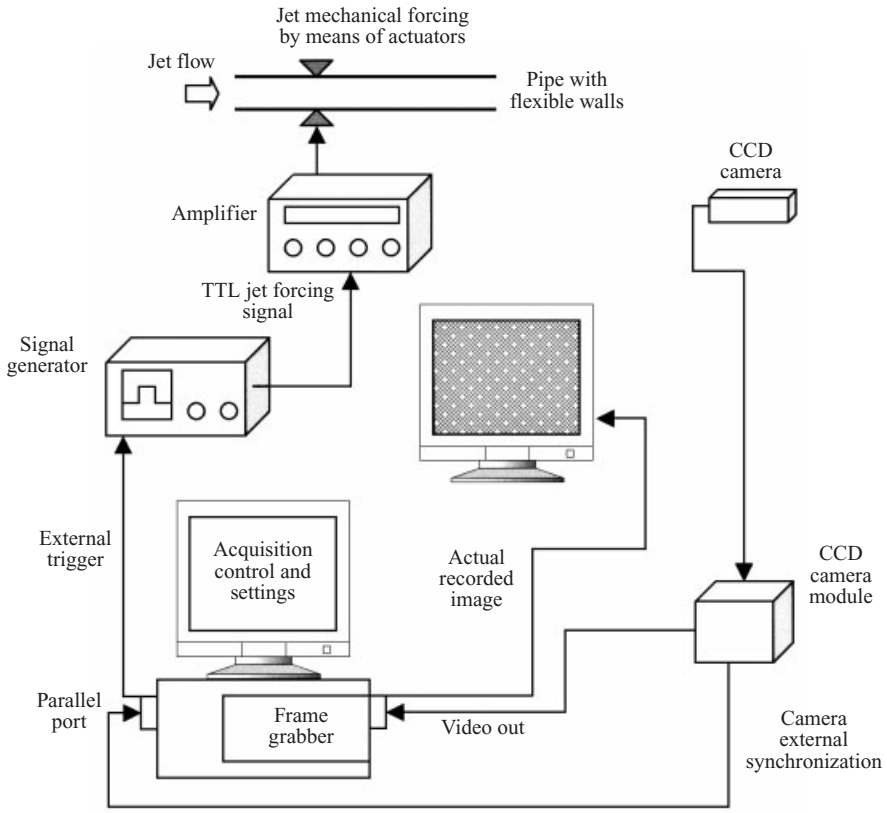



FIGURE 7. The experimental set-up adopted for the conditional acquisitions.

## 4. Results and discussion

### 4.1. *Jet curvature*

The effect of the velocity ratio $R$ is first analysed from a global viewpoint by the study of the jet axis curvature variation. This methodology does not differ from the more standard one developed by Chassaing *et al.* (1974) who determined the jet axis as the locus of the velocity maxima.

An increase of $R$ leads to a decrease of the jet bending with a lower curvature of the jet axis. This effect is studied taking advantage of the longitudinal PIV velocity fields. The integration of the equation of motion, performed by a predictor–corrector algorithm, allows a streamline to be evaluated for a given starting point. The instantaneous streamlines, reported in figure 8, have been obtained as the spatial average on one PIV field of the set of streamlines which originate from a cloud of points located in the jet orifice at fixed $R$. As expected, the streamlines oscillate with small wavelength, owing to the destabilization, whereas the slope is strongly influenced by $R$, with an increase in bending for decreasing $R$.

As proposed by Chassaing *et al.* (1974), the streamline path in the far region can be approximated by a power law function of the form:

$$\frac{y}{D} = A\left(\frac{x}{D}\right)^n. \tag{1}$$

https://doi.org/10.1017/S0022112001007005 Published online by Cambridge University Press

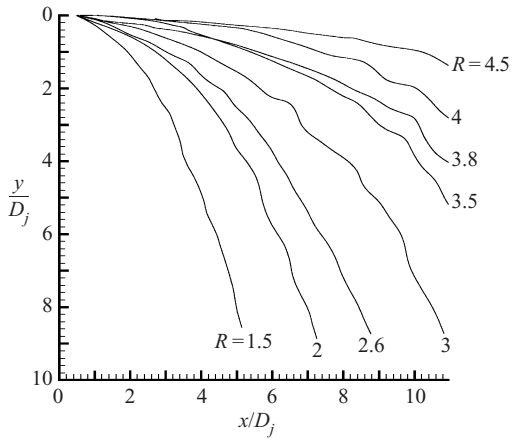



FIGURE 8. Jet streamlines orginating from the jet exit, as functions of the velocity ratio $R$.

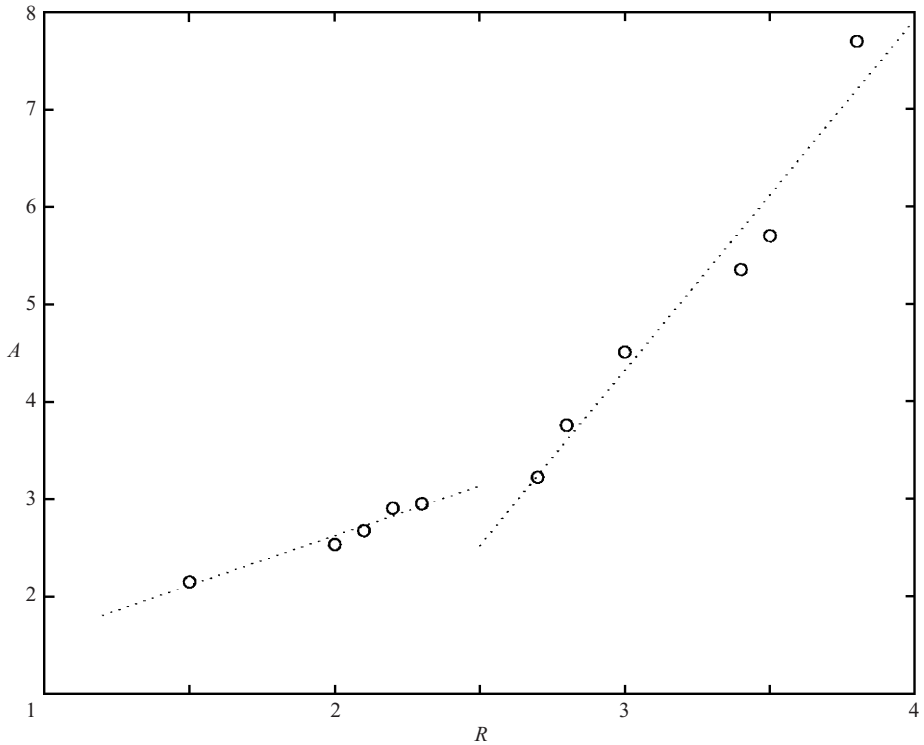



FIGURE 9. Coefficient $A$ of equation (1) as a function of $R$. Two linear fits computed for $R < 3$ and $R \geqslant 3$ are also reported. The use of two fits minimizes the r.m.s. of the experimental points with respect to a single linear fit and a parabolic fit (which has to satisfy the symmetry constraint with respect to $R = 0$).

An exponent $n = 0.39$ about constant with $R$ is found, which was in good agreement with $n = 0.385$ obtained by Chassaing *et al.* (1974) at much larger $Re_j$. Also, the coefficient $A$ of equation (1) is a function of $R$, and the values of $A(R)$, at this low $Re_j$ ($Re_j \simeq 100$), qualitatively show two distinct ranges with linear trends, with a slope variation at $R \simeq 3$ (figure 9). For $R$ smaller than 3, the linear expression is

https://doi.org/10.1017/S0022112001007005 Published online by Cambridge University Press

https://doi.org/10.1017/S0022112001007005 Published online by Cambridge University Press



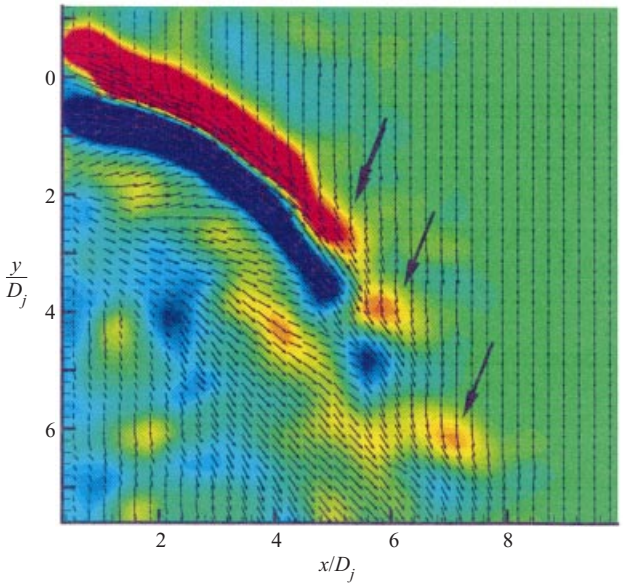



FIGURE 10.

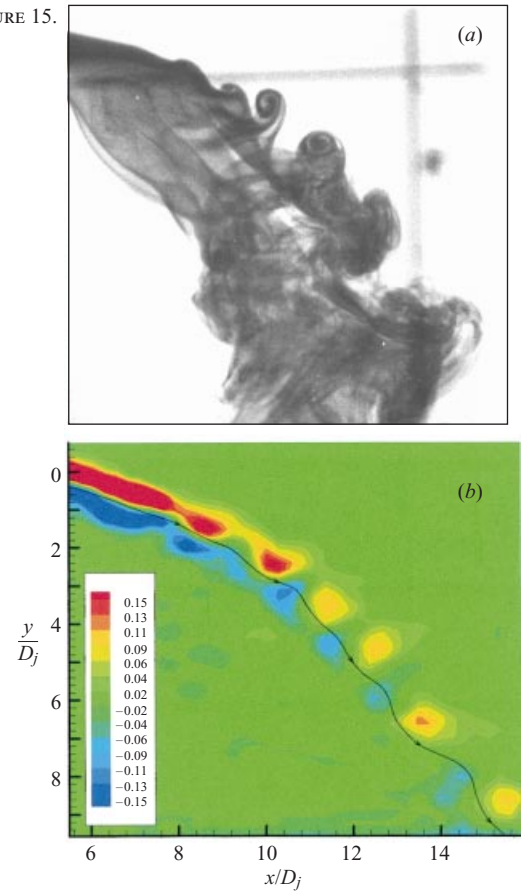



FIGURE 15.

FIGURE 10. Contour plot of the averaged velocity vectors and vorticity amplitude at $R \simeq 2$. Vorticity ranges from −0.1 to 0.1. Red, positive vorticity; blue, negative. The arrows reported in the figures point to three jet-like structures.

FIGURE 15. Longitudinal plane of the jet flow at $R \simeq 3.5$. (*a*) Visualization with blue dye. (*b*) Averaged vorticity contour plot obtained by PIV measurement.



FIGURE 11. LIF longitudinal visualization of the jet flow at $R \cong 2$.

in agreement with that proposed by Chassaing *et al.* (1974). For larger $R$, a slope 3 times larger is found. This result gives a first indication that, depending on the $R$ magnitude, two distinct flow regimes might be noted, $R \simeq 3$ being a transitional value. The presence of two regimes has been observed by Blanchard *et al.* (1999) but in different experimental conditions (a jet with rectangular section) and further discussions on this aspect are given in the following.

### 4.2. *Fluid dynamic regimes*

The variations of $R$ significantly affect the evolution of vortical structures and the interactions among them. In particular, the vorticity content of the ring-like vortices is analysed, showing a probability density function (PDF) which depends strongly on $R$. This feature clarifies the presence of two distinct flow regimes characterized by destabilization mechanisms governed by $R$ and showing significant differences with respect to the instability behaviours expected for free jets.

#### 4.2.1. *Regime identification*

The first important effect of $R$ on the flow behaviour is the change of sign of the RLV structures. According to Andreopulos (1985), the coherent structures emanating from the pipe, carry a vorticity with the same sign as the pipe eddies (jet-like) for all the considered $R$, even at $R = 2$ (as shown by the averaged PIV fields in figure 10). However, at small $R$, eddies with opposite vorticity (wake-like) tend to appear downstream. This behaviour is very well exhibited by a two-dimensional visualization, obtained by the LIF method positioning the laser sheet in the longitudinal plane (figure 11), owing to the ability of the flow visualization to entrain the tracer within the structures having the largest vorticity and associated with the largest pressure drops. The longitudinal visualization of the jet flow filled with blue dye (figure 12)

https://doi.org/10.1017/S0022112001007005 Published online by Cambridge University Press



FIGURE 12. Longitudinal view of the jet flow mixed with blue dye at $R \approxeq 2$.

shows that the jet destabilizes, inducing the formation of the RLV whose azimuthal plane is tilted as an effect of the presence of the wall boundary layer and the cross-stream. Observing figures 11 and 12, it is therefore expected that at low $R$ the negative vorticity of the wake-like structures should be dominant. Furthermore, as shown in figure 10, a vorticity sheet is observed to extend from the vicinity of the jet exit up to about 4 diameters downstream. It seems therefore necessary to assess the nature of the jet-like regions observed in figure 10, in order to understand whether they can be associated with vortical structures rather than with regions of local shear. The presence of vortices, identified as proposed by Robinson (1991), might be visualized by performing a local Galilean transformation (see e.g. Adrian *et al.* 1998) based on the advection velocity of the vortex centroids (Kelso *et al.* 1996). Examples are reported in figure 13. In the case in figure 13($a$), the vector field at $R \simeq 2$ is translated in order to visualize two wake-like vortices formed downstream of the vorticity sheet. In case in figure 13($b$), the translation applied permits jet-like structures to be visualized instead. In both cases, when adopting a proper translation velocity, two structures with negative (figure 13$a$) or positive (figure 13$b$) vorticity are observed from the same velocity field. This analysis requires two distinct advection velocities to be applied, showing that wake-like and jet-like structures move with significantly different velocities. Thus, this result is an indication that their coupling is not as evident as will be inferred at larger $R$.

The quantitative study of the vorticity behaviour at different $R$ has been conducted by the statistical analysis of the vorticity amplitudes $\omega$ over about 50 images (at

https://doi.org/10.1017/S0022112001007005 Published online by Cambridge University Press

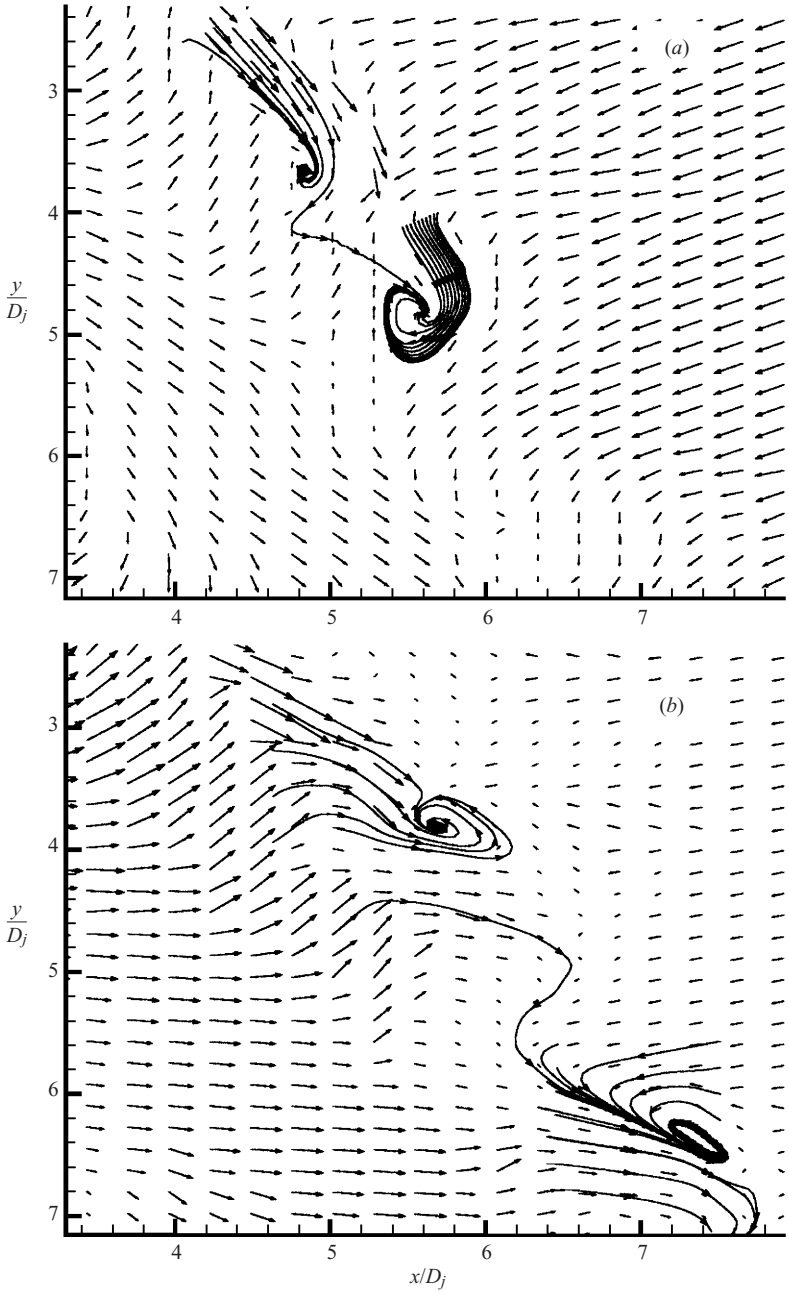



FIGURE 13. Coherent structures educed by proper Galilean transformations of the same velocity field at $R \simeq 2$. (*a*) wake-like structures (adopted translation velocities are $V_x = 1.3\,\mathrm{cm\,s^{-1}}$, $V_y = -1.3\,\mathrm{cm\,s^{-1}}$, (*b*) jet-like structures (adopted translation velocities are $V_x = 0.55\,\mathrm{cm\,s^{-1}}$, $V_y = -1.8\,\mathrm{cm\,s^{-1}}$.

the same $R$). The statistical change of sign of vorticity is clearly demonstrated in figure 14(*a*), where conditional PDFs of the vorticity have been computed by considering only vorticity amplitudes larger than about half the vorticity standard deviation and the background as well as the boundary-layer vorticity contribution is

https://doi.org/10.1017/S0022112001007005 Published online by Cambridge University Press

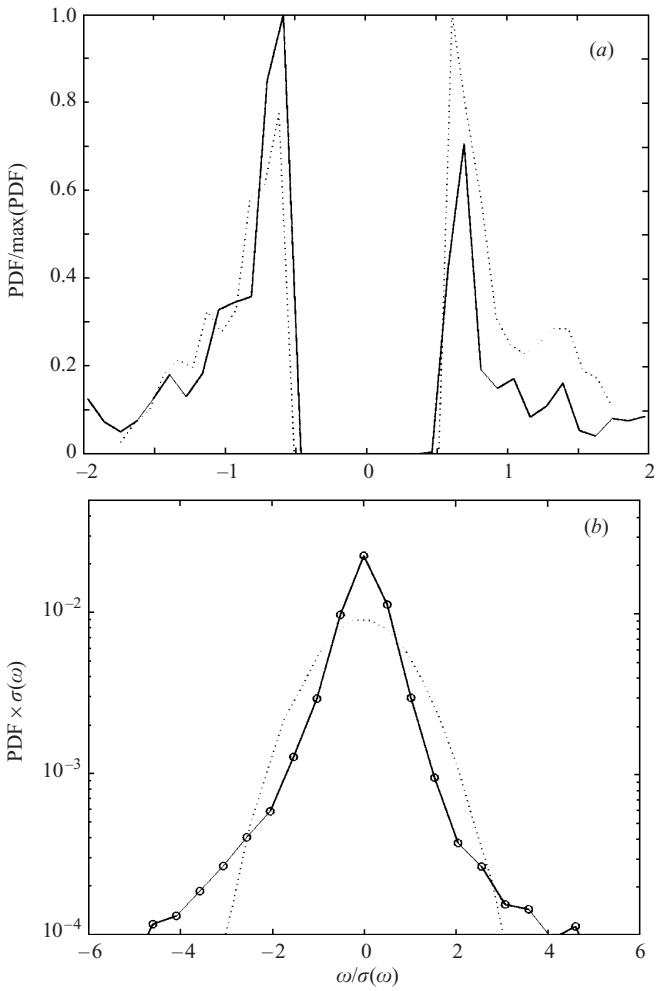



FIGURE 14. Vorticity PDFs. (*a*) Conditional PDFs for ——, $R \simeq 2$; . . . , $R \simeq 3.5$. The amplitudes of the PDFs are normalized with respect to their maximum value, and the $x$-axis with respect to the vorticity standard deviation. (*b*) PDF computed for ——, $R \simeq 2$ compared with . . . , a Gaussian reference. The skewness of the experimental PDF is −0.4 and the flatness is 14.4. Both curves are normalized with respect to the vorticity standard deviation.

no longer included. Thus, the PDF tails contribution is enhanced and it behaves like histograms of sinusoidal functions. The normalization adopted shows the effect of $R$: at low $R$ the wake-like structures dominate (negative vorticity is about 30% larger) whereas an inversion of this trend is observed at larger $R$. At low $R$, the negative vorticity is larger than the positive, thus supporting the idea that the tracer adopted in the visualizations of figures 11 and 12 is entrained mainly within the low-pressure regions associated with the wake-like structures. The vorticity (PDF) obtained for $R \simeq 2$ is reported in figure 14(*b*) superimposed for comparison to a Gaussian PDF with the same standard deviation. The vorticity PDF tails are much larger than the Gaussian ones (e.g. Lesieur 1990) thus yielding a flatness much larger than 3. This behaviour is due to the direct correlation between vorticity and velocity gradients at small scales. Moreover, the PDF is skewed towards negative values giving an

https://doi.org/10.1017/S0022112001007005 Published online by Cambridge University Press

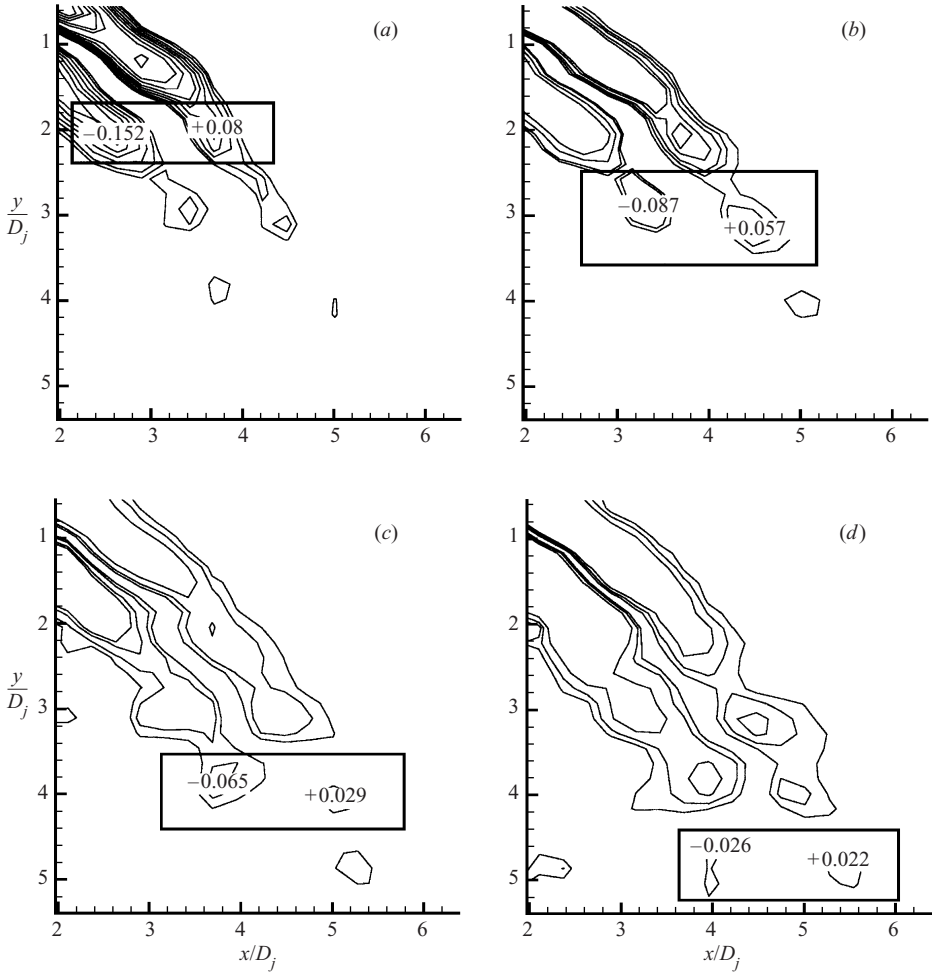



FIGURE 16. Contour plot of the averaged vorticity magnitude for the four different phases at $R = 2$. The images are taken 200 ms apart. The structure examined is shown by the rectangular window, and for each panel the vorticity contour levels have been rescaled so that the selected structure is clearly visible. The reported vorticity amplitudes refer to the maximum positive or negative values within the rectangular window.

indication of the prevailing of wake-like structures (negative vorticity) with respect to the jet-like ones (positive vorticity).

The result of figure 14*a* indicates that jet-like structures at large $R$ should induce an effect analogous to the wake-like structures at small $R$. Examples are reported in figure 15 (p. 125). In figure 15(*a*) a longitudinal flow visualization obtained at $R \simeq 3.5$ is reported. It is observed that jet-like vortices are formed from the jet shear layer and conserve their vorticity sign until a turbulent state is reached. The corresponding PIV result is shown in figure 15(*b*). It is clearly shown that wake-like vortices are indeed present (blue regions) while the vorticity content of the jet-like vorticity structures (red regions) is larger even in the far region. The streamline in figure 15(*b*) originates from the centre of the jet exit so it can be clearly observed that positive vorticity structures belong to the upper side of the jet whereas the negative ones belong to the lower side.

https://doi.org/10.1017/S0022112001007005 Published online by Cambridge University Press

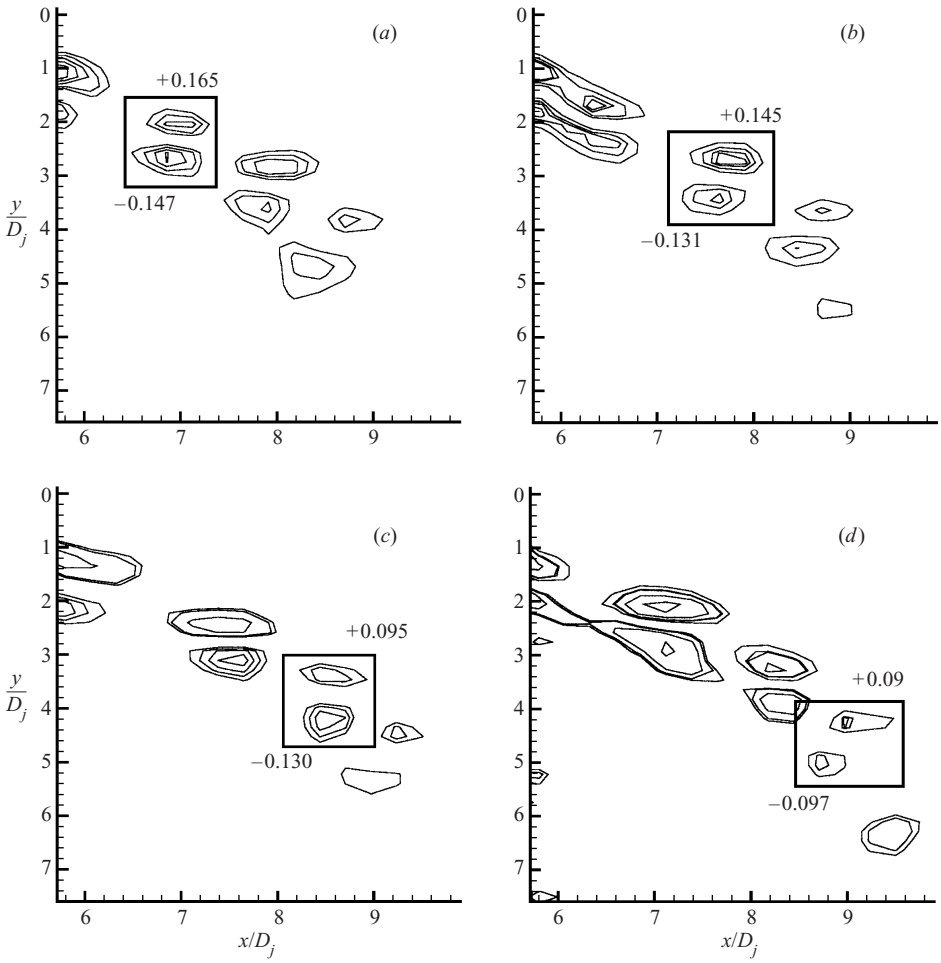



FIGURE 17. As figure 16 but for $R \simeq 3.5$.

The formation and evolution of RLV associated with couples of vortices with opposite vorticity sign, has been examined in detail by the phase-averaging procedure which permits the comparison of averaged flow fields obtained at the four phases considered for the conditional PIV acquisitions. In figure 16, results obtained at $R \simeq 2$ are reported. Taking into account the mean advection velocity magnitude, it is possible to follow the evolution of a single pair of vortices of opposite sign (marked by the rectangular windows in the figure) during the four phases considered, which are separated by a time delay of 200 ms. The vorticity contour plots have been rescaled in each figure so that the same evolving structure can be clearly visualized, and the corresponding maximum vorticity amplitudes are also reported. It is shown that, according to previous discussions, the negative vorticity prevails over the positive at the low $R$ considered, even if, according to Kelso *et al.* (1996), the vortices on the lower side (with negative vorticity) seem to convect more rapidly than those on the upper side.

Results for larger $R$ ($\simeq 3.5$) are reported in figure 17. The presence of pairs of positive and negative vorticity structures is established and they can be clearly associated with signatures of the RLV. According to the statistical analysis performed

https://doi.org/10.1017/S0022112001007005 Published online by Cambridge University Press

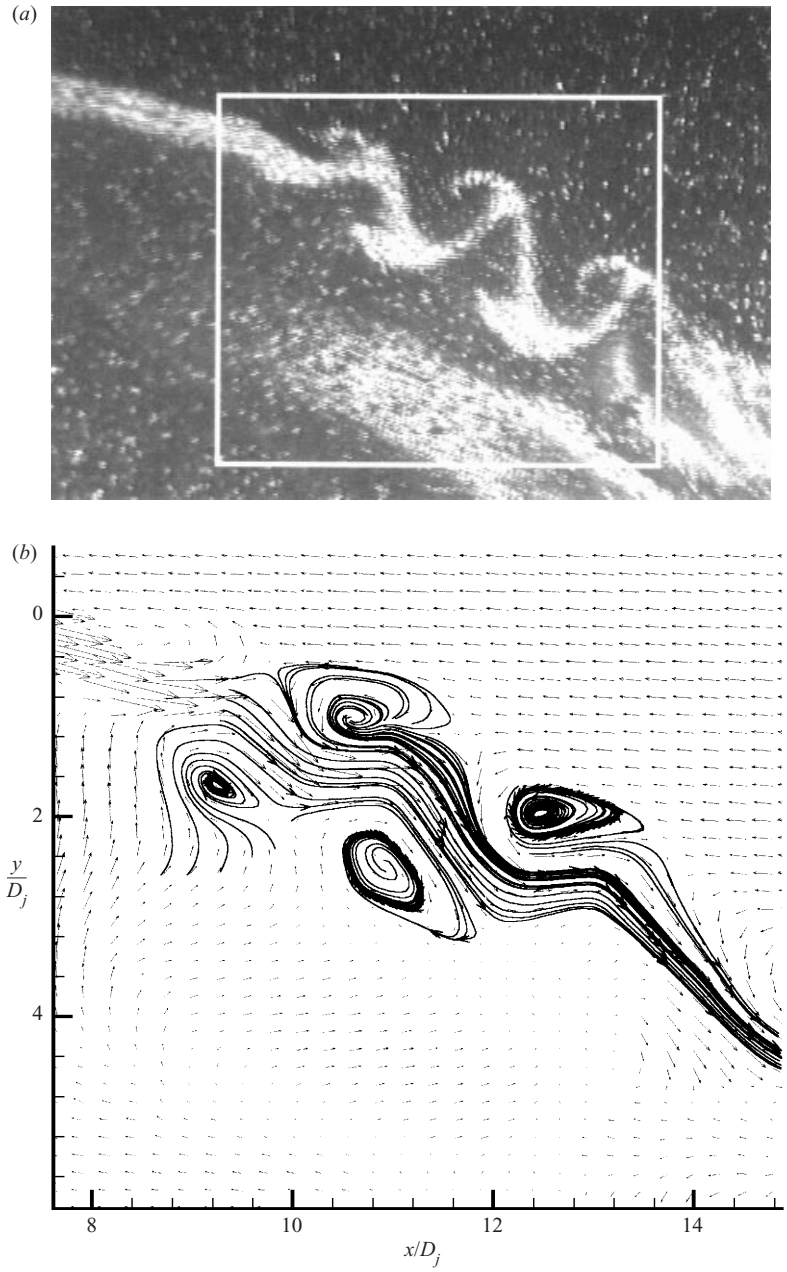



FIGURE 18. (*a*) Mie scattering visualization in the longitudinal plane for $R = 4.5$. (*b*) PIV vector field approximately corresponding to the rectangular region reported in case (*a*). The velocity vector field in (*b*) has been translated (translation velocities are $0.67\,\mathrm{cm\,s^{-1}}$ and $1.33\,\mathrm{cm\,s^{-1}}$ along $x$ and $y$, respectively) and the reported streamlines show the presence of coherent structures.

above, the positive vorticity now prevails, even if the difference between positive and negative vorticity associated with the same structure is not as relevant as for cases at lower $R$. It appears that in the case of figure 17, the vorticity associated with the lower side of the jet decays less rapidly than that of the upper side. This behaviour may be interpreted as an effect of the cross-stream flow whose convective action increases as

https://doi.org/10.1017/S0022112001007005 Published online by Cambridge University Press

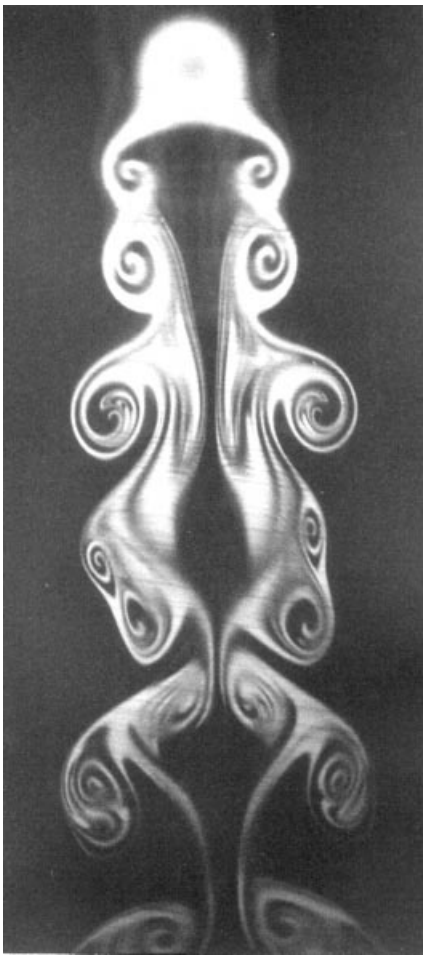


FIGURE 19. LIF visualization obtained by placing the laser sheet parallel and very close to the wall ($x/D_j = 0.2,\ R \simeq 2$).

far as the distance from the jet exit increases, and its effect is more effective on the upper side of the jet.

As $R$ further increases, the coupling between positive and negative vorticity structures becomes more relevant. As an example, in figure 18 a Mie scattering visualization is reported for $R \simeq 4.5$ together with the corresponding PIV relative vector field obtained at a fixed phase. The streamlines traced in figure 18($b$) show the presence of two pairs of vortices which can be associated with two RLVs. The result of figure 18($b$) suggests that positive and negative vorticity structures, which propagate also as an effect of their self-induced velocity, are strongly coupled. This behaviour is quite different with respect to what was observed at lower $R$, thus indicating that the mechanisms leading to the formation of the RLV and the associated destabilization processes of the jet flow, are significantly affected by the $R$ variations.

4.2.2. *The low-R regime*

The different ring-like structure behaviours observed for increasing $R$ may be interpreted in terms of the jet Reynolds number, defined as $Re_{jet} = U_j D_j/\nu$. For

https://doi.org/10.1017/S0022112001007005 Published online by Cambridge University Press

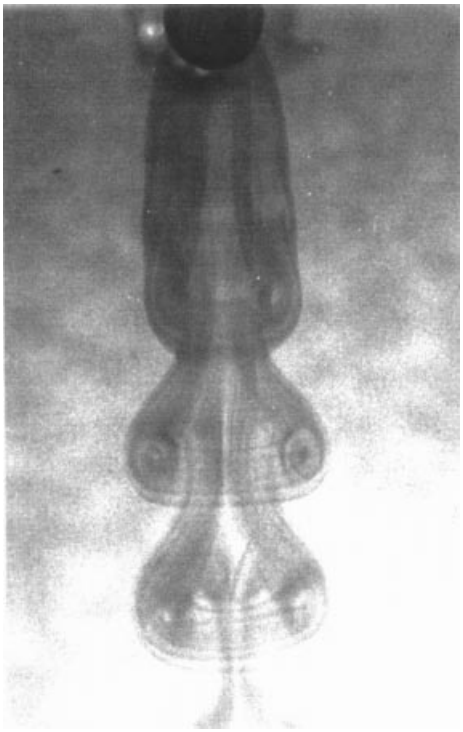


FIGURE 20. Frontal view of the jet flow visualized with blue dye at $R \simeq 2$.

$R \simeq 2$, we obtain $Re_{jet} \simeq 200$ which, for a free jet, is too low to lead to the formation of ring-like structures (Crow & Champagne 1971). Indeed, the jet is characterized by a typical meandering which is deformed by the effect of the cross-stream. According to the interpretation given by Blanchard *et al.* (1999), this behaviour leads to the formation of three-dimensional structures with vorticity dominated by the cross-stream effect and then mainly of negative (wake-like) sign. The three-dimensionality of the structures evidenced by the longitudinal flow visualization and PIV measurements at low $R$, is demonstrated by the transverse flow visualizations at $R \simeq 2$ reported in figure 19. The vortical structures visualized are sections of the bases of the vortical tubes observed in the longitudinal planes. The pairing of two structures and the beginning of a leap-frogging interaction is clearly seen.

A clearer description of the three-dimensional effects is accomplished by the visualization reported in figure 20 obtained with methylene blue dye. It is observed that the formation of annular structures is related to the generation of counter-rotating vortices which cause the separation of the jet flow into two distinct streamwise tubes with vorticity of opposite sign and tangent to the jet axis. At the low $Re_{jet}$ considered here, the jet flow starts to oscillate and such an effect is combined with the pairing of the streamwise CRVP which leads to the formation of the RLV. The wake-like vorticity sign of the longitudinal structures dominating at low $R$ is indeed congruent with the vorticity sign of the CRVP. A scheme clarifying this feature is reported in figure 21. This interpretation is in agreement with observations by Blanchard *et al.* (1999) who described the destabilization mechanisms leading to the formation of the RLV at low $R$ as an effect of elliptical instabilities (see Landmann & Saffman 1987). Furthermore, Leweke & Williamson (1997) analysed the destabilization of parallel

https://doi.org/10.1017/S0022112001007005 Published online by Cambridge University Press

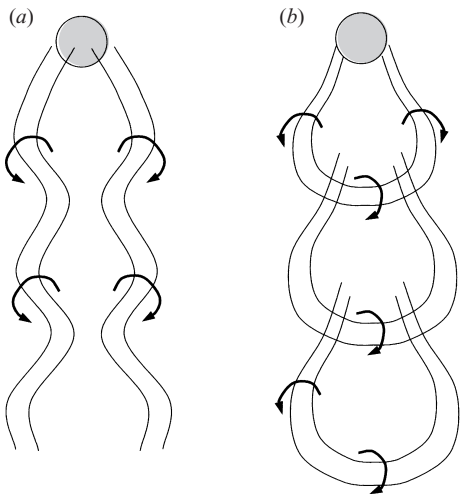



FIGURE 21. A schematic diagram showing the authors' interpretation of the instability process leading to the formation of the ring structures at low $R$. ($a$) Destabilization of the CRVP. ($b$) Pairing and formation of the RLV.

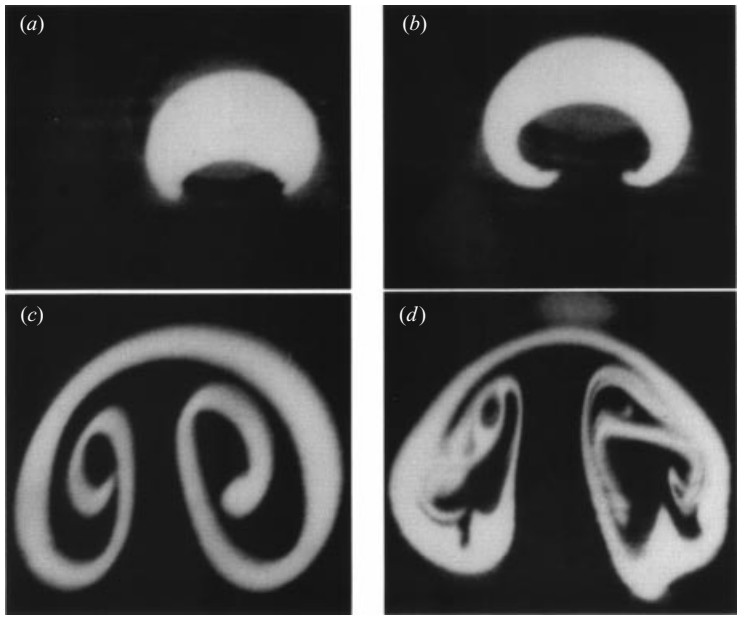



FIGURE 22. Visualization by LIF method of the counter-rotating vortices forming within the jet flow for different distances from the jet exit (the distance increases from ($a$) to ($d$)). The plane of the photograph is perpendicular to the jet axis.

vortex pairs experimentally and showed that short- and long-wavelength elliptical instabilities of the counter-rotating vortices lead to the formation of ring vortices. It is possible from figure 20 to estimate the ratio between the wavelength ($l$) of the CRVP oscillations in the near region preceding the formation of the RLV, and the vortex core diameter ($d_v$). We obtain $l/d_v \simeq 2$ which is in agreement with the value predicted from the elliptic instability theories (Landmann & Saffman 1987).

https://doi.org/10.1017/S0022112001007005 Published online by Cambridge University Press

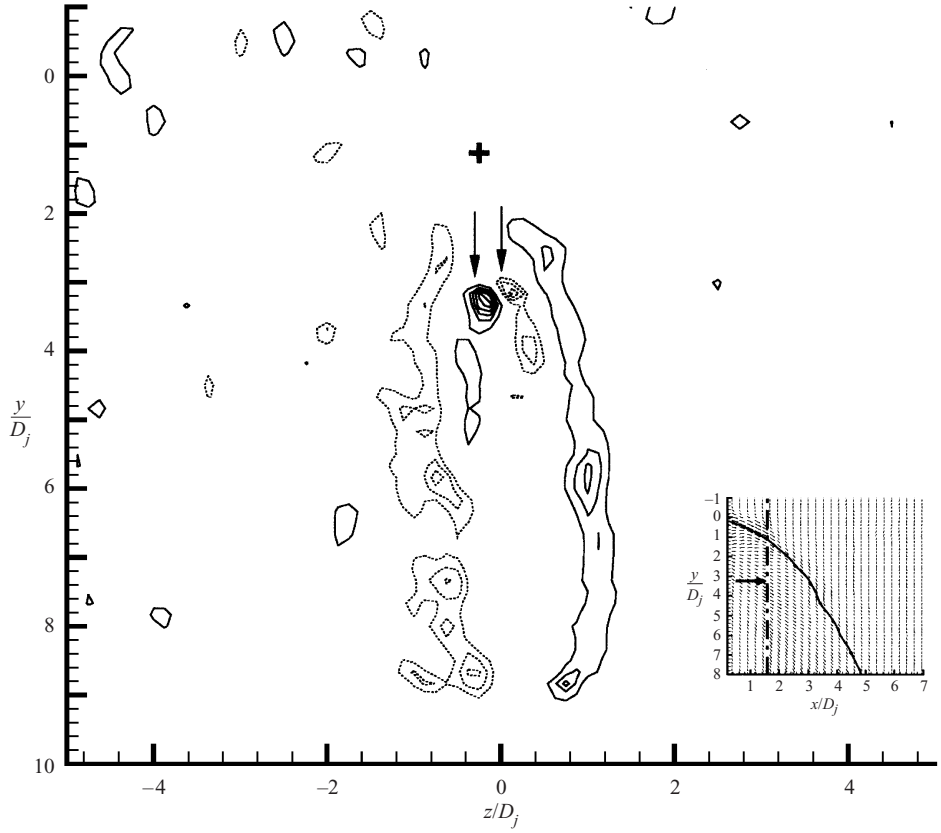



FIGURE 23. Contour plot of the averaged transverse vorticity for $R \simeq 2$ at a distance from the wall $x/D_j = 1.6$. ——, positive vorticity; . . . , negative. The arrows show the presence of the CRVP and the cross is centred on the intersection between the measurement illuminated plane and the streamline originating from the jet exit (from the longitudinal measurement reported in the smaller panel at the same phase and for the same $R$). The arrow in the smaller panel points to the approximate position of the CRVP.

In the present case, the CRVP system is subjected to an external shear due to the transverse current which, as shown in figure 20, induces the tilting and folding of the rotation axis of the annular structures. As pointed out by Andreopulos (1985) the counter-rotating vortices appear as soon as the jet flow starts to bend under the effect of the transverse stream. In figure 22, a sequence of transverse LIF visualizations taken at different distances from the jet orifice and showing the formation and evolution of such vortices is presented for the case $R \simeq 2$. The first case (figure 22*a*) corresponds to the exhaust section whereas the last one (figure 22*d*) corresponds to a distance of about $1.5\,D_j$. According to results at higher $Re_j$, the CRVP tends to form inside the jet just before the fluid reaches the transverse flow (see Coelho & Hunt 1989). According to Moussa *et al.* (1977), it is also observed that the cores of the two coupled vortices destabilize and roll up as far as a fully turbulent state is reached. Greater details can be inferred from the PIV analysis as reported in figure 23. The case reported corresponds to the averaged transverse PIV vorticity field obtained for $R \simeq 2$ and $x/D_j = 1.6$. In the figure, the vorticity contours (solid is positive and dotted is negative) are presented. It is shown that the two counter-rotating structures are clearly determined by the vorticity peak locations (indicated by the arrows) but large

https://doi.org/10.1017/S0022112001007005 Published online by Cambridge University Press

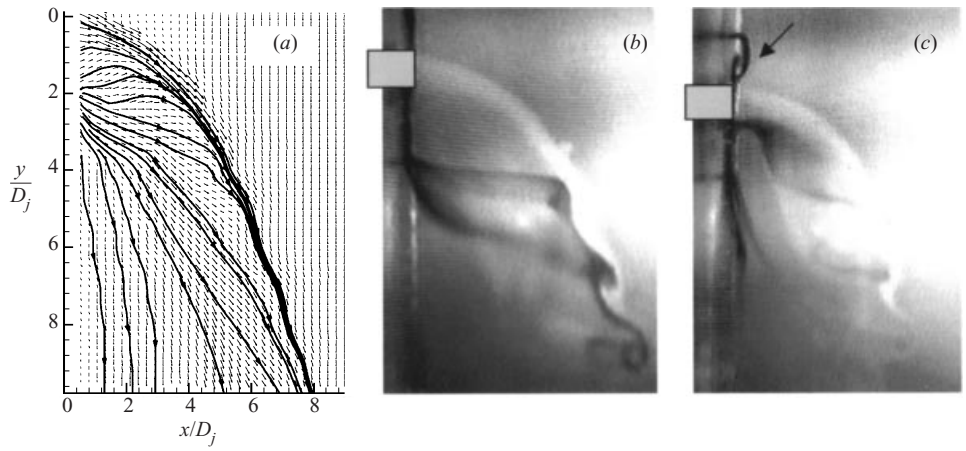



FIGURE 24. Entrainment of wall fluid into the jet at $R \approxeq 2$. (*a*) Averaged PIV vector field. (*b*) visualization obtained with dye injected from the small lateral holes showing the formation of an upright vortex. (*c*) Same as (*b*) but obtained by injecting dye from the upstream small hole. The arrow indicates the formation of the HSV.

regions of shear are also present. Specifically, the vortex with positive vorticity (on the left-hand side of the figure) is surrounded by a negative vorticity sheet while the opposite behaviour is observed for the negative vorticity structure (on the right-hand side of the figure). The analysed section is shown in the longitudinal vector field also given in the figure and corresponding to the same phase of the transverse vector field. It is noted that, according to Blanchard *et al.* (1999), the CRVP is well separated from the jet axis (about 2 diameters downward). The large regions of shear observed in the transverse plane might be explained by the spreading and deformation of the jet shear layer (see also figures 11 and 12). With reference to figures 19 and 20, and owing to the bending of the jet curvature with respect to the transverse measurement plane (see smaller panel of figure 23), the vorticity peaks in the shear regions might be associated to the legs of the RLV which are formed downstream.

It is also evident that the action of the upward vertical velocity induced by the CRVP leads to the entrainment of flow from the wall region up to the RLV. The latter effect is shown in figure 24. In figure 24(*a*) the velocity vectors and streamlines in the region enclosed between the jet flow and the wall ($R \simeq 2$) show the entrainment effect. This behaviour is evident also in figure 24(*b*) where the dye was injected from the lateral holes. The dye feeds the shear-layer vortices, demonstrating that the CRVP induces an upward vertical velocity, of opposite sign with respect to the free stream. This visualization also shows that, in the region bounded by the wall and the jet flow, blue dye coming from the wall seems to be concentrated within vortical structures with vorticity directed quasi-perpendicularly to the wall. The analyses of sequences of images have shown that such structures are unsteady and appear strongly intermittent in time. According to Fric & Roshko (1994), they can be interpreted as prototypes of the upright vortices (UV). Even if only from a qualitative viewpoint, there is a clear indication that the UV, when they are formed, also contribute to feed the jet flow by advecting fluid from the wall region up to the ring-like structures. According to Kelso *et al.* (1996) visualizations, both the UV and the WV therefore contribute to drive boundary-layer flow towards the jet thus feeding the structures formed in its lower shear layer. This confirms the significant interaction between wall structures and jet structures.

https://doi.org/10.1017/S0022112001007005 Published online by Cambridge University Press

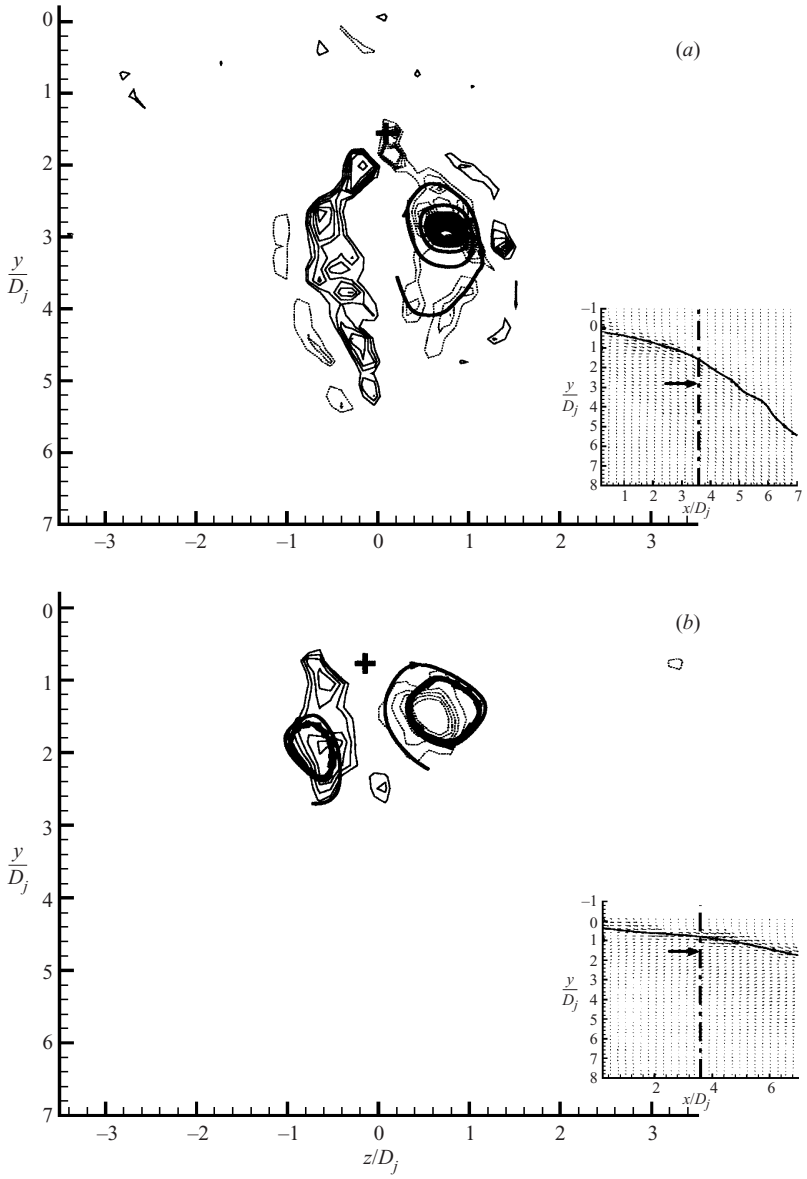



FIGURE 25. Same as figure 23 but for (*a*) $R \simeq 3$ and (*b*) $R \simeq 4$ at a distance from the wall $x/D_j = 3.6$. The solid bold lines are streamlines obtained by translating the vertical velocity of an amount equal to (*a*) $2\,\mathrm{cm\,s^{-1}}$ and (*b*) $1.4\,\mathrm{cm\,s^{-1}}$.

In figure 24(*c*), a flow visualization, obtained by injecting dye from a small hole about 1 diameter upstream the jet orifice, is reported, indicating that fluid coming from upstream is also rapidly entrained. This configuration permits us to identify the presence of an HSV system whose vorticity has the same sign as that of the wall boundary layer.

### 4.2.3. *The high-R regime*

At larger $R$, different mechanisms leading to the RLV formation and to the onset of instability are observed. As reported above (figure 18), and indicated by previous

https://doi.org/10.1017/S0022112001007005 Published online by Cambridge University Press

analyses (e.g. Blanchard *et al.* 1999), the coupling between wake-like and jet-like structures is significant. This behaviour might be again physically interpreted on the basis of the $Re_{jet}$ magnitude which, even for the largest $R$ considered here, is not greater than 1000, which is usually considered the minimum value for the formation of ring structures in axisymmetric jets. As pointed out by Crow & Champagne (1971), the destabilization stage which precedes the formation of isolated puffs might be recognized in the formation of non-symmetrical structures with a crankshaft shape (figure 18*a*) in which the whole jet flow oscillates before the first couple of vortices with opposite vorticity is formed. Such structures are therefore originated by a destabilization mechanism different from the Kelvin–Helmholtz instability of the jet shear layer.

Also in the high $R$ regime, the destabilization mechanisms of the jet flow might be clarified from the analysis of the CRVP signature in transverse planes. The main feature is that the destabilization of the jet is weakly dependent on the $R$ increase, a different trend with respect to destabilization mechanisms of the free jets. In figure 25, examples of the averaged vorticity contour in the transverse plane at $x/D_j = 3.6$, are reported for $R \simeq 3$ and $R \simeq 4$. In figure 25(*a*), the two vortices appear more distorted with respect to the case at larger $R$ but at the same distance from the wall (figure 25(*b*)). The elongation of the vortices should be partially due to the larger angle formed by the jet axis with respect to the transverse measurement plane. In any case, it is evident that the increase of $R$ does not lead to an anticipation of the breakdown. These results will be supported quantitatively in § 5.

In figure 26, the case $R \simeq 4$ at $x/D_j = 5.6$ is reported. The observed behaviour might be interpreted as the final stage of evolution of the counter-rotating vortices. Indeed, the vorticity contour of figure 26*a* shows that two separated structures are no longer visible since they have been completely stretched giving rise to the formation of lateral vortical structures of opposite vorticity and separated from each other by about $2D_j$. It should be stressed that such structures were not observed at lower distances from the wall (figure 25*b*) and, with reference to the smaller panel of figure 26, they appear far downstream along the jet axis which is almost perpendicular to the transverse measurement plane. As shown in the relative vector field of figure 26*b*, they seem to originate as an effect of the velocity induced by the waving of the stretched CRVP.

## 5. Effect of $R$ on the onset of instability

In view of previous arguments, owing to the $Re_{jet}$ magnitude which is never large enough to originate ring-like symmetrical structures, it may be argued that for both low and high $R$, the formation of RLV is not due to a Kelvin–Helmholtz instability process but it is always subsequent to a waving of the jet flow. The jet-flow waving was indeed reflected in the streamline shapes (figure 8) which showed oscillations preceding the RLV formation (see also figure 15*b*). As reported in figure 27, moving along a streamline originating from the jet exit, the waving of the jet is recognized by oscillations of its curvature and the destabilization (i.e. the position where the first RLV is formed) should occur when the curvature radius ($r_c$) is of the same order of magnitude as the length scale of the RLV structures (of the order of $D_j$), whatever the sign of their vorticity. In this way, a quantitative criterion for the determination of the onset of the instability position has been fixed. As an example, with reference to figure 6*a*, the destabilization position corresponding to $r_c/D_j = 1$ leads to $s^* = s/D_j \simeq 3.3$. The destabilization positions ($s^*$) are reported in figure 28 as a function of $R$ showing a linear increase for $R \leqslant 3$, whereas for $R \geqslant 3.5$ they remain

https://doi.org/10.1017/S0022112001007005 Published online by Cambridge University Press

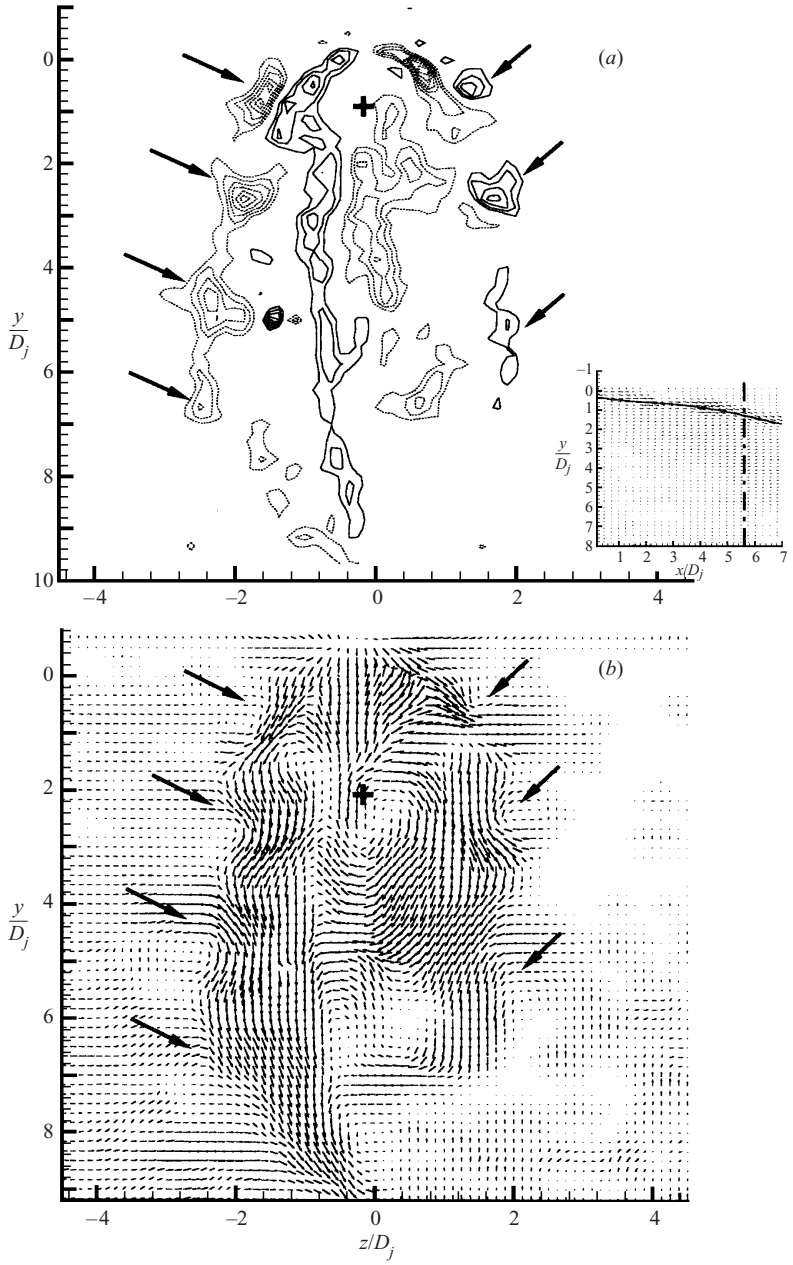



FIGURE 26. Same as previous plot but for $R \simeq 4$ and at a distance from the wall $x/D_j = 5.6$. (*a*) Vorticity contour plot. The arrows point to vortical structures. (*b*) Relative velocity vector field (translation velocity $V_y = 2\,\mathrm{cm\,s^{-1}}$).

about constant. This trend may be explained on the basis of the previous discussion regarding the effect of $R$ on the formation and evolution of the longitudinal structures. Specifically, at low $R$, the longitudinal structures originate from the combined effects of the cross-stream and the CRVP interactions, an effect which, as expected, is delayed for increasing $R$ since the curvature effects become less relevant. We note that this behaviour is opposite to that expected for the instability of the Kelvin–

https://doi.org/10.1017/S0022112001007005 Published online by Cambridge University Press

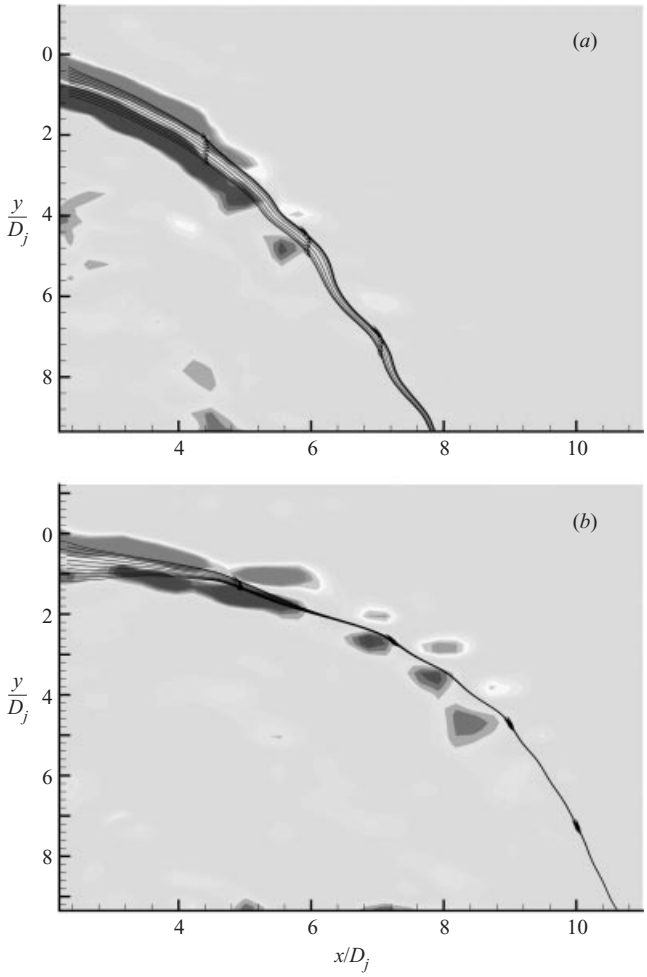



FIGURE 27. Contour plot of the averaged vorticity amplitude obtained by longitudinal PIV measurements at (*a*) $R \simeq 2$ and (*b*) $R \simeq 3.5$. The reported streamlines orginate from the jet exit.

Helmholtz type of free jets where the increase of $Re_{jet}$ leads to an anticipation of the destabilization. On the other hand, for larger $R$, the curvature effects are compensated by the destabilization mechanism proper of the jet flow, so that the location of the destabilization point remains about constant.

## 6. Conclusions

In the present work, the case of a jet exhausting in a cross-stream at a very low Reynolds number ($Re_j \simeq 100$) has been analysed experimentally by means of two- and three-dimensional flow visualizations and phase-averaged PIV measurements. The experiment is conducted in a water tunnel and the flow configurations analysed are varied by changing the velocity ratio $R$ within the range 1.5–4.5.

From a global viewpoint, it is shown that the principal vortical systems which are formed from the interaction of the jet with the cross-stream are the same as those usually observed at larger Reynolds numbers. Specifically, we have documented the generation of the CRVP, observed to rise up inside the jet and the formation of closed

https://doi.org/10.1017/S0022112001007005 Published online by Cambridge University Press

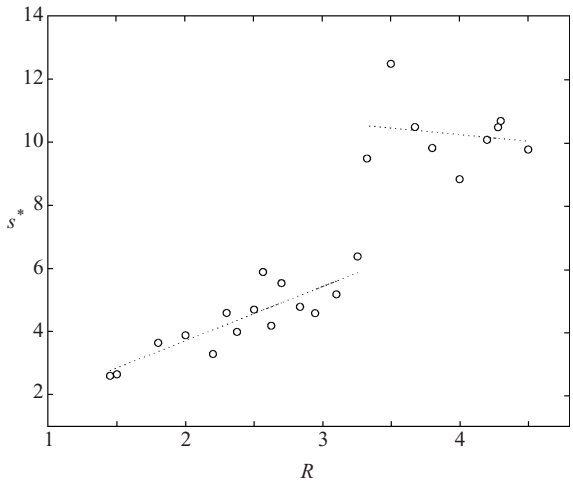



FIGURE 28. Destabilization point as a function of $R$. The non-dimensional curvilinear abscissa $s^* = s/D_j$ denotes the position along the streamline orginating from the jet exit where the criterion $r_c = D_j$ is satisfied. Dashed lines represent linear fit.

structures (the RLV) from the jet shear layer, which are tilted and folded under the influence of the cross-stream. It has been shown that wall fluid is entrained within the jet flow and that at low $R(R \simeq 2)$ unsteady wall structures, interpreted as wake vortices, are also present and interact with the jet flow. Quantitative analyses have also shown that the way the jet axis is distorted and evolves for increasing distances from the jet exit, is in agreement with previous results at larger $Re_j$. The global analysis therefore suggests that, even if quite complicated, the physical characteristics of the vortical structures forming in the cross-flow configuration are independent of the $Re_j$ adopted. Therefore, it is straightforward to argue that numerical simulations at low Reynolds number might be successful for studying this flow configuration.

The low $Re_j$ adopted permitted us to analyse in more detail features connected to the vorticity dynamics. Attention has been focused on the large-scale vortical structures with azimuthal (RLV) and axial vorticity (CRVP), and on their evolution for increasing $R$.

The main result obtained is the detection of two distinct flow regimes whose characteristics depend on the $R$ magnitude, with $R \simeq 3$ being a transitional value.

At low $R(R < 3)$, the longitudinal vorticity is dominated by the so-called wake-like structures which carry vorticity of opposite sign with respect to the equivalent structures forming in free jets. It is observed that the longitudinal structures with wake-like vorticity are three-dimensional vortices which are generated by the CRVP meandering and pairing. A possible explanation of such a mechanism is found in the elliptical instability of the vortex pair. In the low $R$ flow regime it is indeed observed that the destabilization of the jet flow which drives the formation of the ring-like vortical structures is associated with oscillations of the jet axis and it is delayed for increasing $R$. The instability mechanism which leads to the formation of the RLV seems therefore to be dominated by the jet axis curvature effects combined with the pairing of the counter-rotating vortices, being the Reynolds number proper of the jet too low to induce on the jet shear layer any instability of Kelvin–Helmholtz type. In this sense, in the low $R$ regime, the RLV usually observed by the visualizations might be considered as a product of the CRVP destabilization and are constituted of jet

https://doi.org/10.1017/S0022112001007005 Published online by Cambridge University Press

fluid. Secondary vortices with jet-like vorticity in the longitudinal plane and coupled to the RLV exist, but they are formed of fluid coming from the cross-stream being unable to entrain jet fluid.

In the high $R$ regime ($R > 3$), the so called jet-like structures are statistically dominant and for $R \simeq 4$, the larger jet Reynolds number reached is reflected in the strong coupling between the jet-like and wake-like vortices. In this case, the curvature effects and the CRVP evolution are observed to play a less stringent role for the RLV formation. In the final stage of the jet evolution, a central role seems still to be played by the pair of counter-rotating vortices. It is observed that, for fixed distance from the wall ($x/D_j$), an increase of $R$ weakly affects the CRVP destabilization, such a trend being in agreement with the delayed formation of the ring-like structures for increasing $R$.

Therefore, in both the low and high $R$ flow regime, the destabilization mechanisms are driven by the CRVP and the jet flow is unable to induce Kelvin–Helmholtz instabilities on the shear layers.

The authors acknowledge the Department of Mechanics and Aeronautics of the University 'La Sapienza' of Rome, for having rendered available the experimental facilities. F. Stella, G. Franco and A. Leone are sincerely acknowledged for their help during measurements and T. Kowalewski for his fruitful support in the development of the PIV system. The work was supported by grants from CNR (1996 and 1999).

## REFERENCES

Adrian, R. J. 1991 Particle imaging techniques for experimental fluid mechanics. *Annu. Rev. Fluid Mech.* **23**, 261–304.

Adrian, R. J., Christensen, K. T., Soloff, S. M., Meinhart, C. D. & Liu, Z. C. 1998 Decomposition of turbulent fields and visualization of vortices. *Proc. 9th Intl Symp. on Applications Lasers to Fluid Dyn.* 16.1.1-8, *Lisbon, 13–16 July*.

Andreopulos, J. 1985 On the structures of jets in cross-flows. *J. Fluid Mech.* **157**, 163–197.

Andreopulos, J. & Rodi, W. 1984 Experimental investigation of jets in a cross flow. *J. Fluid Mech.* **138**, 93–127.

Blanchard, J. N., Brunet, Y. & Merlen, A. 1999 Influence of a counter rotating vortex pair on the stability of a jet in a cross flow: an experimental study by flow visualizations. *Exps. Fluids* **26**, 63–74.

Broadwell, J. E. & Breidenthal, R. E. 1984 Structure and mixing of a transverse jet in incompressible flow. *J. Fluid Mech.* **148**, 405–412.

Cenedese, A. & De Angelis, G. 1998 Near field analysis of a jet in cross flow by means of LIF and PTV. *Proc. 8th Intl Conf. on Flow Visualisations*, (*paper* 203) *Sorrento, 1–4 September*.

Chassaing, P., George, J., Claria, A., & Sananes, F. 1974 Physical characteristics of subsonic jets in a cross-stream. *J. Fluid Mech.* **62**, 41–64.

Coelho, S. L. V. & Hunt, J. C. R. 1989 The dynamics of the near fields of strong jets in a cross flow. *J. Fluid Mech.* **200**, 95–120.

Crow, S. W. & Champagne, F. H. 1971 Orderly structures in jet turbulence. *J. Fluid Mech.* **48**, 547–591.

Fearn, R. & Weston, R. P. 1974 Vorticity associated with a jet in a cross flow. *AIAA J.* **12**, 1666–1671.

Fornalik, E., Nakabe, K., Yamamoto, Y., Chen, W. & Suzuki, K. 1999 Visualizations of heat transfer enhancement regions modified by the interaction of inclined impinging jets into crossflow. *Mach. Graph. Vis.* **8**, 597–610.

Fric, T. F. & Roshko, A. 1994 Vortical structures in the wake of a transverse jet. *J. Fluid Mech.* **279**, 1–47.

Hiller, W., Koch, S., Kowalewski, T. A. & Stella, F. 1993 Onset of natural convection in a cube. *J. Heat Mass Transfer* **16**, 3251–3263.

https://doi.org/10.1017/S0022112001007005 Published online by Cambridge University Press

Kamotani, Y. & Greber, I. 1972 Experiments on a turbulent jet in a cross flow. *AIAA J.* **10**, 1425–1429.

Keane, R. D. & Adrian, R. J. 1992 Theory of cross-correlation analysis of PIV images. *Appl. Sci. Res.* **49**, 191–215.

Kelso, R. M., Lim, T. T. & Perry, A. E. 1996 An experimental study of round jets in cross flows. *J. Fluid Mech.* **306**, 111–144.

Krothapalli, A., Lourenco, L. & Buchlin, J. M. 1990 Separated flow upstream of a jet in cross-flow. *AIAA J.* **28**, 414–420.

Landmann, M. J., & Saffman, P. G. 1987 The three dimensional instability of strained vortices in a viscous fluid. *Phys. Fluids* **30**, 2339–2342.

Leweke, T. & Williamson, C. H. K. 1997 Cooperative elliptic instability of a vortex pair. *J. Fluid Mech.* **360**, 85–119.

Lesieur, M. 1990 *Turbulence in Fluids*, 2nd edn. Kluwer.

McMahon, H. M., Hester, D. D. & Palfery, J. G. 1971 Vortex shedding from a turbulent jet in a cross-wind. *J. Fluid Mech.* **48**, 73–80.

Moussa, Z. M., Trishka, J. W. & Eskinazi, S. 1977 The near field in the mixing of a round jet with a cross stream. *J. Fluid Mech.* **80**, 49–80.

Quenot, G. M., Pakleza, J. & Kowalewski, T. A. 1998 Particle image velocimetry with optical flow. *Exps. Fluids* **25**, 177–189.

Raffel, M., Willert, C. & Kompenhans, J. 1998 *Particle Image Velocimetry*. Springer.

Robinson, S. K. 1991 Coherent motions in the turbulent boundary layer. *Annu. Rev. Fluid Mech.* **23**, 601–639.

Smith, S. H. & Mungal, M. G. 1998 Mixing, structure and scaling of the jet in crossflow. *J. Fluid Mech.* **357**, 83–122.

Willert, C. E. & Gharib, M. 1991 Digital particle image velocimetry. *Exps. Fluids* **10**, 181–193.

https://doi.org/10.1017/S0022112001007005 Published online by Cambridge University Press